Synthesis and growth mechanism of Bi2O2CO3 nanosheets by pulsed discharges in liquids

Anna Nominé Nominé, M. Nazarov, Thomas Gries, C. Noel, Jaâfar Ghanbaja, Alexandre Nominé„ A Nominé, F. Brochard, V. A. Milichko, T. Belmonte

Synthesis and growth mechanism of $Bi_2O_2CO_3$ nanosheets by pulsed discharges in liquids

A.V. Nominé[1], M. Nazarov[1,2], T. Gries[1], C. Noel[1], J. Ghanbaja[1], A. Nominé[1,3], F. Brochard[1], V. Milichko[1,3], T. Belmonte[1,*]

1. Université de Lorraine, CNRS, IJL, F-54000 Nancy, France
2. Lomonosov Moscow State University, Leninskie gory 1 bld. 3, 119991 Moscow, Russia
3. ITMO University, St. Petersburg 197101, Russia

* thierry.belmonte@univ-lorraine.fr

Keywords

Discharges in liquids ; Nanoobjects ; growth mechanism ; non-equilibrium ; nanowalls ; nanosheets

ABSTRACT

The growth of $Bi_2O_2CO_3$ nanosheets through nanosecond-pulsed discharges in liquid environments has been achieved by applying voltages slightly above the breakdown voltage. This growth process involves surface modification of the cathode electrode following pretreatment with chemical etching. Remarkably, the choice of liquid medium, whether water or liquid nitrogen, does not significantly affect the interaction between the electrodes and the metallic discharge that forms during the initial stages of synthesis. This process is template-free. The anisotropic growth of these two-dimensional objects is attributed to ion-assisted deposition via the ledge mechanism, supplemented by the presence of surface defects. Prior to the growth treatments, chemical etching is essential to enhance the probability of nanosheet formation from virtually zero to almost a hundred percent. This step is crucial in eliminating native oxide layers and exposing surface defects, which are present as parallel planes forming combs within polishing scratches. The detachment of nanosheets from the cathode and their release into the liquid is facilitated by the sweeping of the liquid-bubble interface, which breaks the nanosheets away from their substrate. As the electrodes undergo aging, nanosheets are formed by outward diffusion of bismuth and reaction with water and CO_2 in the air. By gaining a better understanding of this growth mechanism, exciting opportunities arise for the design and large-scale production of 2D nanostructures.

1. Introduction

Intense research efforts have focused on 2D materials due to their exceptional properties and potential to unveil novel phenomena [1-3]. However, the utilization of discharges in liquids for nanosheet production is uncommon for most materials (except for carbon), which are often absent from comprehensive reviews in the field [4-8]. Notably, while significant progress has been made in generating various types of nanocarbons through experiments with arc discharges in gas, the synthesis of nanosheets composed of non-carbon materials has remained relatively limited, following the pioneering work by Sano *et al*. [9, 10].

Nanosheets growth through nanosecond-pulsed discharges in liquids has proven successful for various materials such as ZnO [11], AgO [12], and PbO_2 [13]. Hamdan *et al*. [14] achieved the formation of 2D mesoporous CuO agglomerates by assembling elementary nanocrystals with sizes in the range of a few nanometers. Saito *et al*. [15] generated SnO plates through a discharge initiated in a 0.001 M K_2CO_3 solution, utilizing a biased Sn wire operating at 400 V. The anisotropic nature of these nanostructures is attributed to differential growth rates, resulting in the formation of $Sn_6O_4(OH)_4$ octahedrons that

assemble into plate-like skeleton crystals. In these studies, the electrodes contribute the necessary material for the formation of nanoobjects through their erosion.

Similarly, Chen *et al*. [16] utilized a gas-liquid interface discharge at atmospheric pressure between two tungsten electrodes. One electrode was positioned above a 0.1 mol/L $NaNO_3$ solution, while the other was immersed in the liquid. They successfully synthesized ultrathin single-crystal WO_3 nanosheets consisting of six monolayers. This achievement was accomplished through the lateral attachment of small WO_3 nanocrystals. In a similar setup, Furuya *et al*. [17] synthesized gold nanoplates; however, the metal source was not the electrodes but rather $HAuCl_4$ (0.33 mM) added to an aqueous solution containing 1.33 mM $NaHCO_3$. These structures formed on the surface of the solution, rather than within the solution itself. Recently, a rapid synthesis of Mn_3O_4 nanosheets was achieved through a one-step liquid plasma discharge deposition. This process involved orienting a titanium foil perpendicularly to the electric field created between two electrodes placed in an electrolyte. The electrolyte consisted of 0.01 M $C_4H_6MnO_4 \bullet 4H_2O$, 0.5 M NaCl, 9 mg of (1-Hexadecyl) trimethylammonium bromide as a surfactant, and 50 mL of deionized water mixed with 30 mg of polyvinylpyrrolidone as a stabilizing agent [18]. Notably, no nanosheets could be grown when the electric field was parallel to the surface of the foil.

$Bi_2O_2CO_3$, a nanostructured material with unique layered structures, is composed of alternate stacking of $(Bi_2O_2)^{2+}$ sheets interleaved by CO_3^{2-} groups [19]. It exhibits exceptional photocatalytic properties when exposed to UV–vis light irradiation [20, 21]. Consequently, $Bi_2O_2CO_3$ has garnered considerable attention in the field of photocatalysis until recently [22-28]. It can be hybridized with various elements or cocatalysts such as Bi [29, 30], Br [31], Ni [32, 33], BiOCl [34], g-C_3N_4 [35-37], RGO [38], polyaniline [39], Ag_2CO_3 [40] Bi_2MoO_6 [41], Bi_2WO_6 [30], MoS_2 [42], Mo_2S_3 [43], Co_3O_4 [44] or Fe_2O_3 [45].

$Bi_2O_2CO_3$ nanosheets can be synthesized using various methods, including hydrothermal and solvothermal processes [19, 46], sonochemical synthesis [47], electrochemical exfoliation of bismuthene [48], or controlled reconstruction of SN-BiO_x immersed in a 0.5 M $KHCO_3$ solution [49]. Among these methods, the production of nanoobjects through pulsed discharges in liquids stands out as a versatile one-pot synthesis process, capable of anchoring nanoparticles and generating hierarchical nanostructures [50, 51]. Furthermore, it is highly efficient, enabling the production of tens of milligrams of nanoobjects per hour [52].

In this paper, we aim to elucidate the growth mechanism of nanosheets through nanosecond-pulsed discharges in liquids when the metal is introduced through electrode erosion. We utilized bismuth electrodes, which were immersed in both liquid nitrogen and water, as the source material for the formation of bismuth nanosheets. Following synthesis, these nanosheets underwent oxidation and transformation into $Bi_2O_2CO_3$ through CO_2 reaction from the air.

2. Experimental details

The experimental setup was described in detail in a previous publication [53]. In summary, the setup involved a solid-state switch (Behlke HTS-301-03-GSM) connected to one pin-electrode, while the other electrode was grounded. The switch was supplied by a high DC voltage power generator (Technix SR15-R-1200-15 kV-80 mA). The voltage rise time was approximately 20 ns. Pulses of positive voltage, with a duration of 75 ns, were applied at a frequency of 10 Hz to the power electrode (anode) for a duration of 30 minutes. The influence of the applied voltage was investigated in the range of +4 to +10 kV. Nanosheets were formed only when the voltage was slightly higher than the breakdown voltage, around 4 kV for liquid nitrogen and milli-Q water. Specifically, nanosheets were synthesized at +4 and +5 kV, with the highest production observed at +5 kV. Beyond this voltage, nanoparticles are

synthesized and all the more numerous as the voltage increases. At +10 kV, nanosheets are no longer synthesized. All results presented in this study were obtained at +5 kV.

The experimental setup involved immersing the two electrodes, configured in a pin-to-pin arrangement, in a 100 mL Dewar flask for liquid nitrogen and in a 30 mL glass beaker for water. The distance between the electrodes was maintained at a constant 100 µm throughout the process using micrometric screws for continuous adjustment. This setup allowed for repeated breakdown to occur. Nanosheets were prepared using either liquid nitrogen (99.9998% purity) or milli-Q water (with a resistivity of 18.2 MΩ·cm). The synthesis process involved an ultra-facile and rapid procedure consisting of the following steps:

- Pre-treatment: The electrodes underwent chemical etching in a selected etching solution.
- Treatment: The electrodes were subjected to erosion using nanosecond-pulsed discharges in either liquid nitrogen or water.
- Exposition to air: For liquid nitrogen, once the liquid had evaporated, the nanosheets were exposed to air. For water, the nanosheets were collected in the solution and exposed to air.

The bismuth rods used as electrodes were obtained from Goodfellow Ltd. They had a diameter of 10 mm and were of high purity, with a 99.999% purity level. To prepare the electrodes, they were first sharpened to form conical tips (see **supplemental material 1**). Then, they were polished using a 1200-grit sanding disk and rinsed with tap water. Subsequently, the electrodes underwent chemical etching in a selected etching solution for a duration of 20 minutes. After etching, they were rinsed with distilled water, mounted on holders, and immersed either in liquid nitrogen or milli-Q water.

Various etching solutions (see **supplemental material 1**) were prepared using Nitric Acid (70%) from Sigma-Aldrich Co., ethanol (99.8%, AR) from VWR International LLC, acetic acid, chloric acid, and iron (III) chloride. Comparable results were obtained using all of these solutions. The results presented in this study were obtained after etching using the Nital-5% solution.

After the treatment process and complete evaporation of the liquid in the case of liquid nitrogen, nanosheets were collected through sedimentation. A TEM (transmission electron microscopy) holey carbon grid was placed on a silicon wafer at the bottom of the vessel to capture the nanosheets. These collected nanosheets on the TEM grid and silicon wafer were then available for further analysis. In the case of liquid nitrogen, nanosheets underwent oxidation only when exposed to air, and this oxidation process was uncontrolled. However, when synthesized in water, the oxidation occurred in the liquid phase. The resulting nanosheets had a lamellar structure. With exposure to air, carbonation occurred through the reaction of CO_2, transforming the bismuth oxide into $Bi_2O_2CO_3$. This process has not to be confused with the aging of the electrode material as discussed hereafter. Carbonation is very fast as it is observed after a few seconds whereas aging takes days. The former is only observed on the cathode, whereas the latter affects both electrodes.

To investigate the structure and composition of the nanosheets, high-resolution transmission electron microscopy (HRTEM) was conducted. The characterization was performed using a JEOL ARM 200F cold FEG TEM/STEM equipped with a GIF quantum ER model 965, operating at 200 kV with a pixel resolution of 0.12 nm. High-angle annular dark-field scanning transmission electron microscopy (HAADF-STEM) and two-dimensional elemental mapping using energy-dispersive X-ray spectroscopy (EDX) were employed to determine the chemical composition of the nanoparticles. Additionally, scanning electron microscopy (SEM) observations were carried out using an FEI Quanta 600 FEG SEM.

An ultrafast camera FASTCAM SA5 (model 1000K-M3) was used to observe the discharge bubble and the release of nanosheets in the case of water. Videos were recorded at a rate of 75 000 frames per second with a pixel resolution of 12.3 µm.

Slow-mode recording at 60 images per second was also used to observe the liquid flow.

3. Results and discussion

The pre-treatment is not mandatory for obtaining nanosheets, but this step significantly enhances the likelihood of obtaining them, increasing the probability from nearly zero to nearly 100%. As previously mentioned, it has been observed that the applied voltage should not be excessively high, but rather slightly higher than the breakdown voltage. All etching solutions appear to yield similar outcomes, making them indistinguishable. The process produces about 5 mg of nanosheets in 30 min.

Characterization of nanosheets

The structure and composition of individual nanosheets were investigated by different methods. In **Figs. 1a-c**, HR-TEM images, diffraction patterns and simulated structures of nanosheets are provided when the objects are observed along the [110], [010] and [001] zone axes. For the two first cases (**Figs. 1a** and **1b**), this required to select nanosheets presenting a cross section of their thickness oriented perpendicularly to the electron beam. **Fig. 1d** shows a larger view of such a nanosheet, which is correctly oriented to be analyzed along the axes of its cross-section plane. We observe the characteristic zigzag structure of the $Bi_2O_2CO_3$ phase along the [010] zone axis as described by several authors [54-56]. X-ray diffraction patterns of large sets of nanosheets could also be interpreted with this structure, by using the JCPDS file 41-1488 (**supplementary material 2**).

Electron Energy Loss Spectroscopy was also used to analyze the various forms of carbon associated with the nanosheets. **Fig. 1e** shows the presence of C=O and C-O bonds, which are found in the carbonate group, demonstrating the incorporation of CO_2 molecules from the air in the structure of the bismuth oxide. Energy-filtered elemental maps of Bi, O and C elements, showed in **Fig. 1f**, show the homogeneous distribution of these elements in a nanosheets.

AFM measurements (**supplementary material 3**) made on multiple nanosheets showed that the average thickness of the thinnest single (unstacked) nanosheets is around 3 nm with a relatively smooth surface, showing an amplitude of ±0.3 nm.

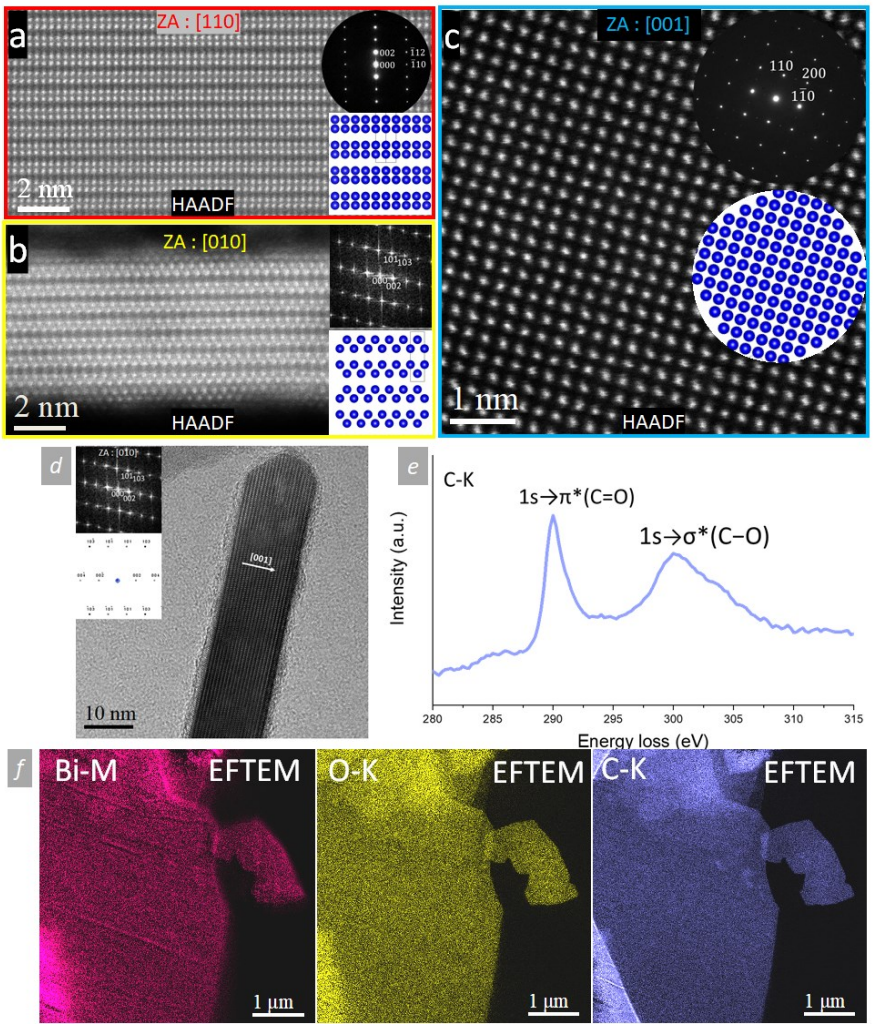

Fig. 1: HR-TEM images, diffraction patterns and simulated structures of cross-sections of nanosheets with a) [110] zone axis and b) [010] zone axis. c) HR-TEM image and diffraction pattern of the top side of the selected nanosheet along the [001] axis. D) larger view of a HR-TEM image of the cross-section of a nanosheets with the corresponding FFT spectra. e) Electron energy loss spectrum of a nanosheet at the Carbon K-edge. d) Energy-filtered elemental maps of Bi, O and C elements.

The most remarkable discovery regarding nanosheets is their consistent characteristics (shapes, compositions, structures, etc.) regardless of whether they are synthesized in liquid nitrogen or water (**see Fig. 1**). Bismuth oxide nanosheets exhibit various shapes depending on their thickness, regardless of the liquid medium. When they are sufficiently "thin" (*i.e.*, below ~5 nm, otherwise considered "thick"), they can appear flat, crumpled, or rolled due to stress (**Figs. 2a-c** in liquid nitrogen and **Figs. 2e-g** in water). On the other hand, thicker nanosheets maintain a flat configuration (**Fig. 1d** and **1h**). Single nanosheets (see circles in **Figs. 2a**, **2d**, **2e** and **2h**) distinctly show the presence of kinks.

During treatment times of 30 minutes, the most abundant structures are thin crumpled nanosheets (**Figs. 2b** and **2f**), with a smaller number of thin flat nanosheets (**Figs. 2a** and **2e**). However, their reprocessing by the discharge is likely responsible for their fragmentation into smaller parts (**Figs. 2d** and **2h**). Thin rolled nanosheets (Figs. 1c and 1g) are rarely observed, and the reason for their adopting this geometry remains unknown.

Scanning electron microscopy images in the **supplementary material 4** provide an overview, revealing the presence of crumpled nanosheets. Upon closer examination at high magnification, small fragments

similar to those depicted in **Figs. 2a** and **2e** can be easily observed around the crumpled nanosheets. Additionally, thick nanosheets, such as those shown in **Figs. 2d** and **2h**, can be seen broken due to stress.

This stress is induced by oxidation and the uptake of CO_2 from the air. Remarkably, the nanosheets presented in this study exhibit identical size, shape, composition, and crystallographic features as those reported by several authors [34, 46, 48, 54, 55] (refer to **supplemental material 5**). They consist of stacked layers with a zig-zag structure, constituting a 2D material. As explained by Zhang *et al*. [34], CO_2 can convert BiOOH into $Bi_2O_2CO_3$. This aspect will be discussed in detail hereinafter.

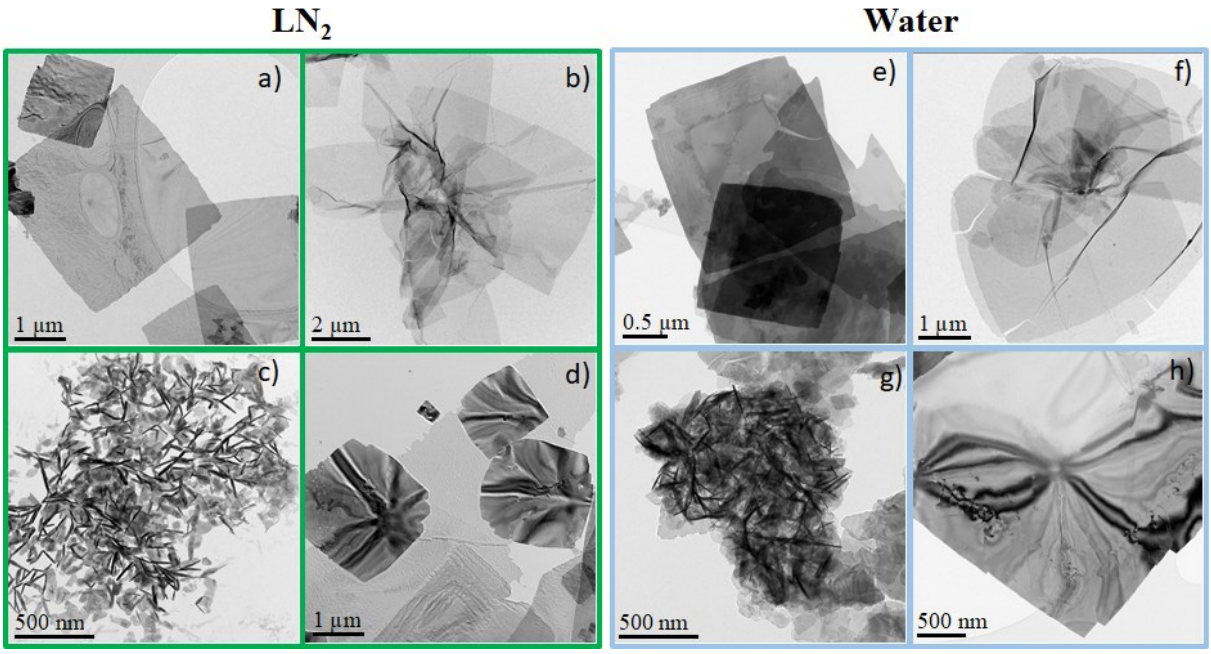

Fig. 2: Bright Field TEM micrographs showing the different shapes of nanosheets synthesized in liquid nitrogen and in water. a) and e) thin flat nanosheets. b) and f) thin crumpled nanosheets. c) and g) thin rolled nanosheets. d) and h) thick flat nanosheets. Circles show the presence of kinks.

Metallic character of discharges

The ability to use either water or liquid nitrogen equivalently can be attributed to two possibilities: either different growth mechanisms are at play, or if the mechanisms are the same, similar discharge conditions are being implemented. To compare the emission spectra obtained from time-resolved optical emission spectroscopy in the two liquids, refer to **Fig. 3**. It should be noted that the data collected in water were slightly noisier compared to those obtained in liquid nitrogen (as mentioned in a previous work [56]). The optical fiber used for these measures was not directly plunged in the liquid like it could be done in LN_2, which is more insulating than water. Despite this difference, the presence of bismuth lines (indicated by "o" in **Fig. 3**) is clearly observed and identified from the time-resolved spectra (refer to **supplemental material 6**, where the absence of Hα emission at 656 nm is also noted). Furthermore, the lack of OH emission, as demonstrated in **supplemental material 7**, provides strong evidence of the metallic nature of the discharges.

The absence of H and OH emissions in the spectra obtained in water, even long after breakdown when the medium is optically thinner, indicates that the discharge is predominantly metallic and arises from the emission of metal vapor resulting from electrode erosion. The emitted vapor displaces the water, leading to a discharge that closely resembles what is observed in liquid nitrogen.

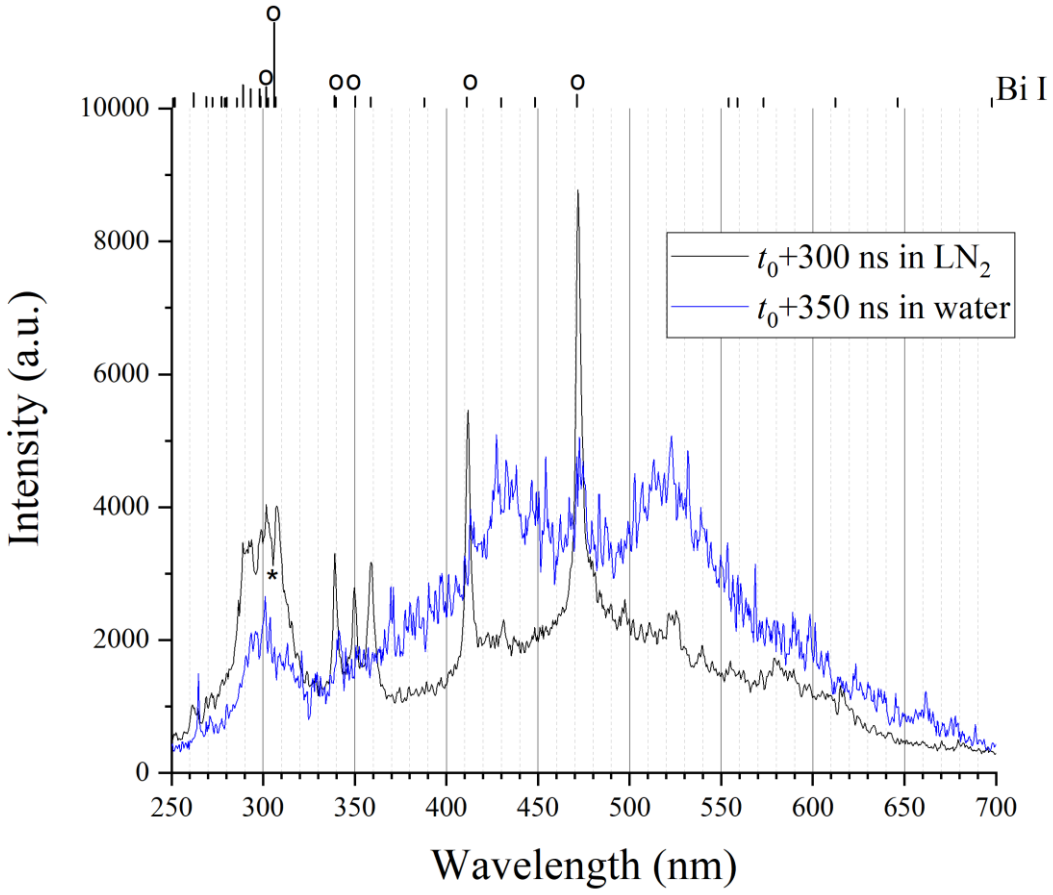

Fig. 3: Comparison of low-resolution emission spectra recorded by time-resolved optical emission spectroscopy in water and in liquid nitrogen at almost the same times after breakdown (t_0). Before 300 ns in water, only continua are observed (150 ns in liquid nitrogen). Spectra in water are much noisier than in liquid nitrogen. For this reason, Bi I lines that are identified for certainty are depicted by an "o" above the expected wavelengths of the possible transitions showed by bars on the top of the graph. * shows an absorbed line due to absorption of photons emitted by the continuum. Data in liquid nitrogen were taken from [56]. Wavelengths of Bi I transitions are taken from NIST [57].

Aging in air

Following the treatment, the electrodes were subjected to aging in ambient air for 6 days. Let's mention first that the aging of $Bi_2O_2CO_3$ nanosheets from the solution does not change these objects at all. On the contrary, the surface states of both electrodes change as BOC nanosheets grow by this process. Thus, the colour of the electrodes turns to white.

The results are shown in **Fig. 4**. After 6 days, the surfaces of the electrodes were found to be completely covered with ultra-large nanosheets, measuring approximately 100 µm in width (**Fig. 4a**). The trenches resulting from the polishing process were barely visible as they were concealed by the nanosheets (**Figs. 4b**). The kinetics of the direct oxidation of bismuth in air, both in dry and moist conditions, as well as in superheated steam, have been investigated at temperatures above 500 K [58]. However, these oxidation processes are too slow to be measured at room temperature. Hence, it is presumed that an alternative mechanism is responsible for the observed phenomenon in the present study.

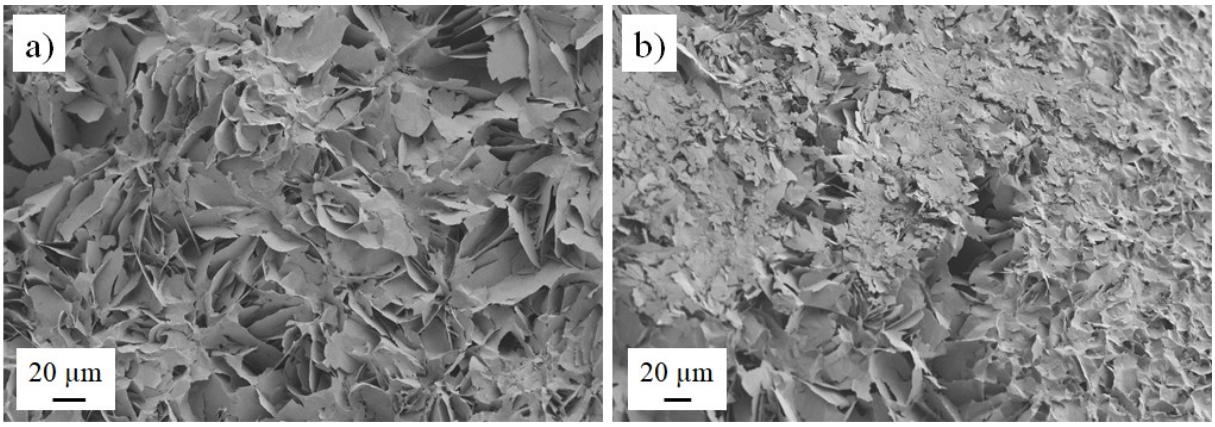

Fig. 4: $Bi_2O_2CO_3$ nanosheets formed in the air after 6 days. a) Detail of the basal nanosheets. b) Image showing two trenches and nanosheets covering the gap between them.

Subsequently, experiments were conducted to examine whether similar outcomes could be achieved without in-liquid discharge treatment. These experiments involved electrode polishing, Nital etching, and exposing the electrodes to air for a duration of 6 days as well. The result shows undoubtedly that no nanosheets were synthesized without in-liquid discharges (**supplemental materials 8**).

Surface states of the electrodes

After the treatment, the electrode tips exhibit two distinct regions: one covered by impacts and the other covered by trenches resulting from the polishing and etching steps (refer to **supplemental material 9**). Following the polishing process (**Figs. 5a-c**), the scratches on the surface appear as flat streaks that are almost connected, with minimal spacing between them. Upon etching (**Figs. 5d-f**), clear trenches with widths ranging from 0.5 to 1 µm become visible. The chemical etching of the electrodes facilitates the formation of these trenches on the surface. The dissolution of the native bismuth oxide, which may have varying thickness locally, leads to differential erosion of the surface, increasing its roughness. In **Fig. 5f**, one can observe the presence of closely spaced parallel planes forming comb-like structures, which are a result of the chemical etching process. This feature is also evident in **Figs. 5h** and **5i**. After the treatment (**Figs. 5g-i**), the trenches are still observable, measuring approximately 3-5 µm in width. Within these trenches, numerous localized and aligned nanostructures consisting of entangled nanosheets form flower-like patterns, but only on the cathode. No flowers are observed on the anode, and this observation holds true for both liquids (refer to **supplemental material 10**). The random distribution of these nanostructures along the scratches is attributed to the presence of localized defects, likely the planes of the comb structures, which promote their growth. This mechanism is a result of a deposition process rather than a solid-diffusion process like oxidation, as observed in both water and liquid nitrogen. It can be concluded that the bismuth forming the flower-like structures can only originate from the vapor produced by the erosion of the electrode tip.

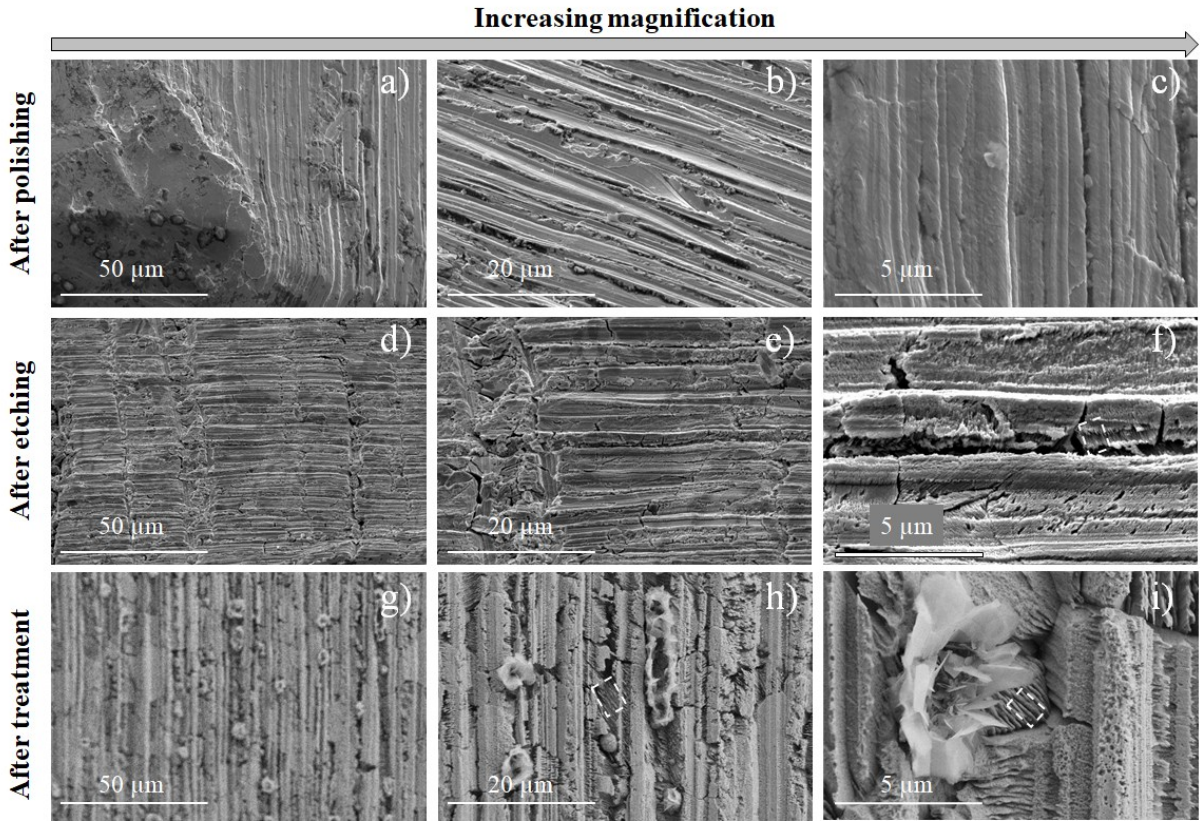

Fig. 5: Surface states of the bismuth cathode at different magnifications after: polishing, chemical etching and discharge erosion (here in liquid nitrogen). Areas enclosed by rectangles with dashed lines in f), h) and i) show the presence of tight parallel plans forming combs (see also **Fig. 5** for higher resolution images).

Figures 5a-e illustrate examples of flower-like structures formed within the trenches. These structures are composed of entangled nanosheets. Upon close observation, it is evident that the largest and thinnest nanosheets do not stand upright but spread out over the surface (**Fig. 6a and 6e**). The flowers grow perpendicular to the surface within the trenches (**Fig. 6c**) and on the comb structures (**Fig. 6b**). This growth pattern suggests that the process involved is deposition rather than etching. Notably, the growth of nanosheets on the comb structures appears to be influenced by the orientation of the underlying planes (**Fig. 6d**), as the nanosheets align accordingly.

Possible growth supports

Within the present process, several surfaces are involved, including the liquid-air interface, the interface between the gas bubble and the liquid, and the surfaces of the electrodes. While it is occasionally possible to observe nanosheets floating on the surface of water, it remains uncertain whether this phenomenon is also applicable to liquid nitrogen, as the surface of the liquid is typically rough. However, in most cases, nanosheets are denser than the liquid and tend to collect at the bottom of the vessel. The ability of nanosheets to float is attributed to changes in the buoyancy force resulting from an increase in liquid uptake within the nanostructures [59]. Depending on the sign of the buoyant mass, which may vary over time, colloidal particles either sediment towards the bottom or rise towards the surface. In both cases, gravity creates a density gradient of particles in the vertical direction. Sedimentation-diffusion equilibrium is achieved when the particle flow induced by gravity is balanced by the diffusive flow driven by the density gradient and interparticle interactions. Therefore, at initial stages, nanosheets do not grow at the air-liquid interface. This observation is supported by slow-mode

videos that reveal the trace left by erosion products in the liquid (refer to **supplemental material 11**). Consequently, this mechanism can be ruled out as the primary mode of nanosheet growth at the air-liquid interface.

The possibility of nanosheet growth at the interface between the gas bubble and the liquid can also be ruled out. If nanosheets were synthesized at this interface, there would be no need for a pre-treatment step. The emission of vapor from the electrodes, heated by the discharge, would remain unchanged regardless of whether a pre-treatment was performed or not. Consequently, condensation of vapor atoms on the bubble-liquid interface would occur consistently. However, it should be noted that the erosion process of the electrodes caused by the arc discharge is not influenced by the thickness of the native oxide layer, which is typically a few nanometers thick at room temperature. This thickness is significantly smaller compared to the depth of the crater left by the discharge under the present conditions, which is approximately 1 µm [53].

Therefore, it can be concluded that nanosheets can only grow on the surface of the electrodes, and it is observed that this mechanism exclusively occurs on the cathode.

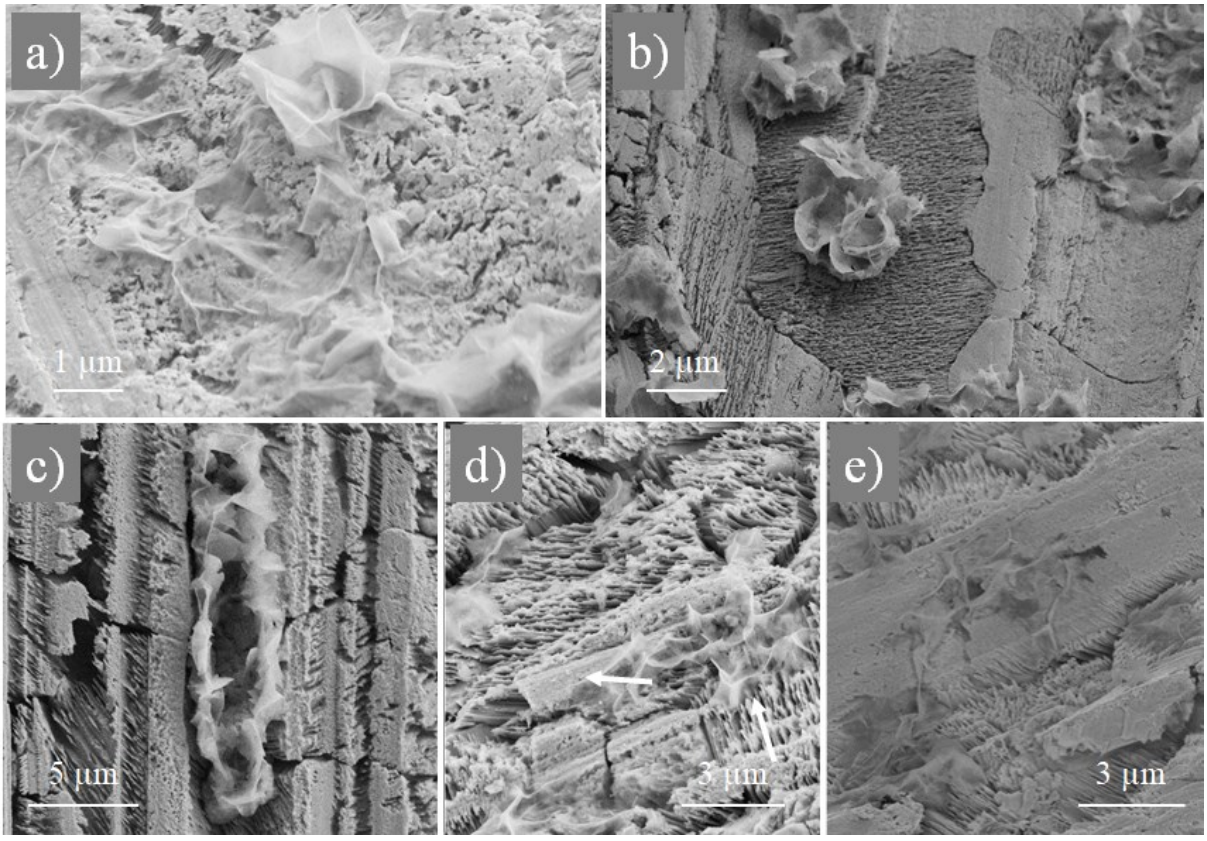

Fig. 6: Example of flowers of nanosheets observed on the surfaces of cathodes. a) Network of nanosheets with one flower. Note that no nanosheets stand on the smooth surface on the left-hand side of the image. b) Flowers are located on rough areas like combs. c) flower growing along walls in one trench. Note the orientation of the combs on either side of the trench. d) Nanosheets on combs with two different orientations (given by arrows). e) Nanosheets spreading from a trench on a smooth surface.

Transfer to the liquid

Through the utilization of an ultrafast camera with high resolution (refer to **supplemental material 12**), we were able to observe that the transfer of nanosheets from the surface of the cathode to the

liquid is facilitated by the mechanical sweeping action of the bubble-liquid interface (**Fig. 7**). This phenomenon occurs during an event where the bubble undergoes a single expansion and collapse (**Fig. 7a**), and the release of nanoobjects can be witnessed following the collapse phase (**Fig. 7b**). The velocity distribution of the released nanoobjects narrows around the mean fluid velocity, indicating a deceleration of their movement after being ejected from the bubble.

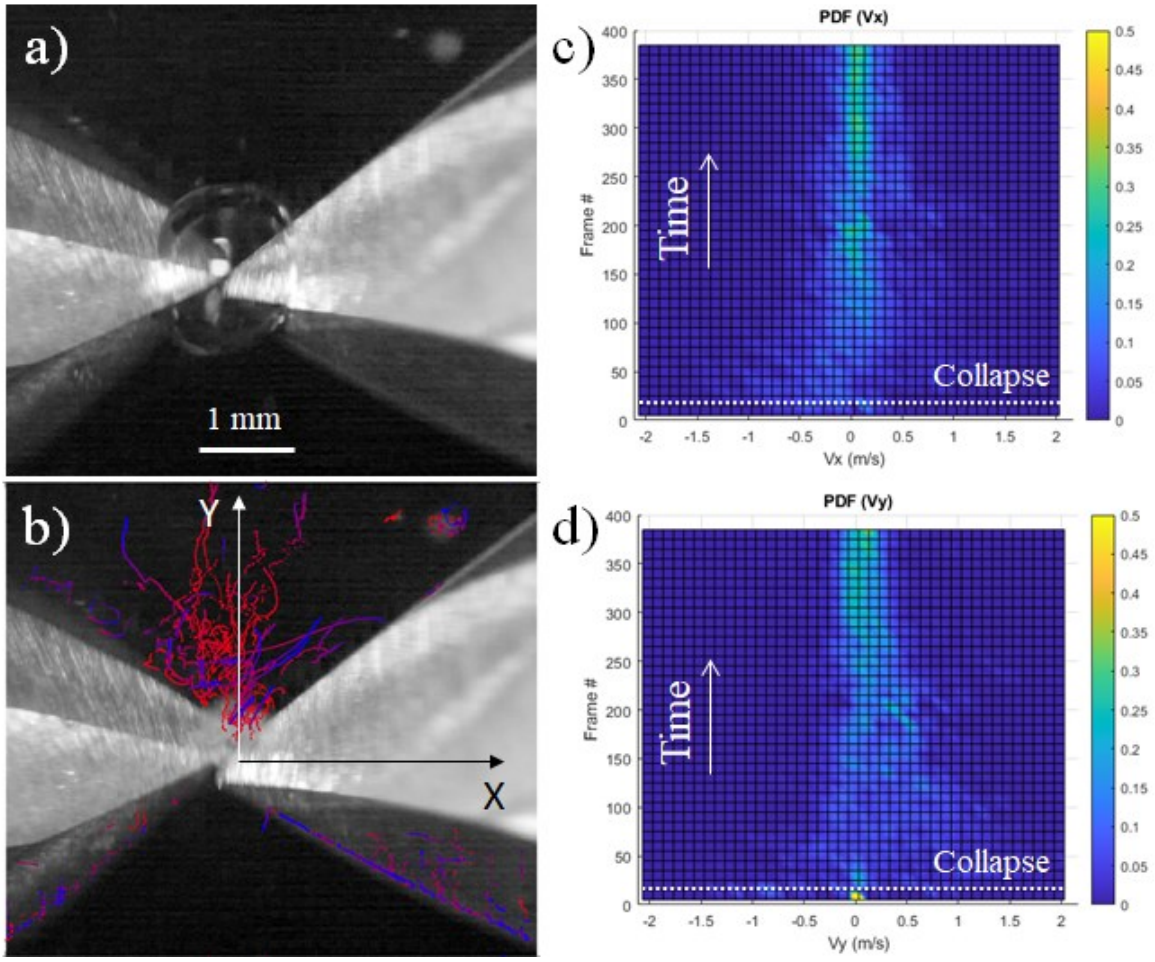

Fig. 7: a) Image of the bubble collapse 53 µs after breakdown. b) Trajectory of nanoobjects tracked after the collapse in the liquid (integration over 990 frames recorded every 13.3 µs, *i.e.* 13.2 ms). The red-to-blue scale corresponds to the first 400 frames where changes are the most significant. c and d) Normalized Probability Density Function (PDF) of the velocities of the tracked nanoobjects projected onto the horizontal and vertical axes, respectively. The end of the bubble collapse is shown by a dotted line. The velocity distribution strongly narrows around the mean value of the fluid velocity, which is slow and close to 0. This evolution shows the slowing down of movement of the nanoobject after ejection from the bubble.

Indeed, this mechanism of mechanical sweeping by the bubble-liquid interface is responsible for the fragmentation of nanosheets into smaller pieces. It explains the presence of small fragments alongside flowers or parts of flowers. However, the precise factors that control the thickness of the nanosheets remain to be fully understood. Recently, Gupta *et al*. [47] successfully synthesized 2D $Bi_2O_2CO_3$ nanoobjects through a sonochemical method. By employing various suspension media such as water, methanol, isopropanol, ethanol, and an isopropanol:water (4:1) mixture, they were able to manipulate the lateral sizes of the nanoobjects, ranging from micrometer-sized nanosheets to nanoflakes measuring tens of nanometers. Experimenting these liquids with the present process could be useful

for comparison with Gupta *et al.*'s results, even though the use of liquid nitrogen and water already demonstrates the lack of sensitivity of the present process to the chosen liquid. Further research is needed to confirm the underlying mechanisms that govern the thickness of nanosheets in Gupta *et al.*'s process, but the lack of electrode in their case and the much longer processing times that are needed pleads in favour of another growing mechanism.

Growth mechanism

Nanosheets commonly exhibit kinks, which can be easily observed in **Figs. 2a**, **2d-2f**. This observation led us to consider the "ledge" mechanism, which is well-known for describing the growth of plate-like precipitates within solid matrices [60]. In this context, the matrix is either replaced by the liquid itself, which acts as an isotropic medium, or by a suitable surface capable of supporting the growth of 2D objects.

In the case of precipitation within solids, the growth of the precipitate via the ledge mechanism is driven by the coherency of the interfaces between the precipitate and the matrix where the growth occurs. The development of the precipitate is more significant for incoherent interfaces than for coherent ones. Additionally, the lateral growth of the precipitate typically outpaces its thickening [60]. In the present case, the possibility of replacing the solid matrix with the liquid medium must be ruled out because it would not align with the observed phenomenon of using either water or liquid nitrogen.

Under conditions that are thermodynamically unfavourable, vapor cannot adsorb and adhere to surfaces without additional energy provided by surface defects such as emerging dislocations or atom vacancies. This explains why nucleation on electrodes occurs randomly, where defects are present. Similarly, nucleation on nanosheets is possible as long as these surface defects are present within the nanosheets themselves [61]. **Fig. 8** demonstrates this phenomenon, where a BOC nanosheet serves as a substrate for the growth of a nanopyramid from an emerging screw dislocation. It is worth noting that these types of objects are rare, as nanosheets are typically single crystals.

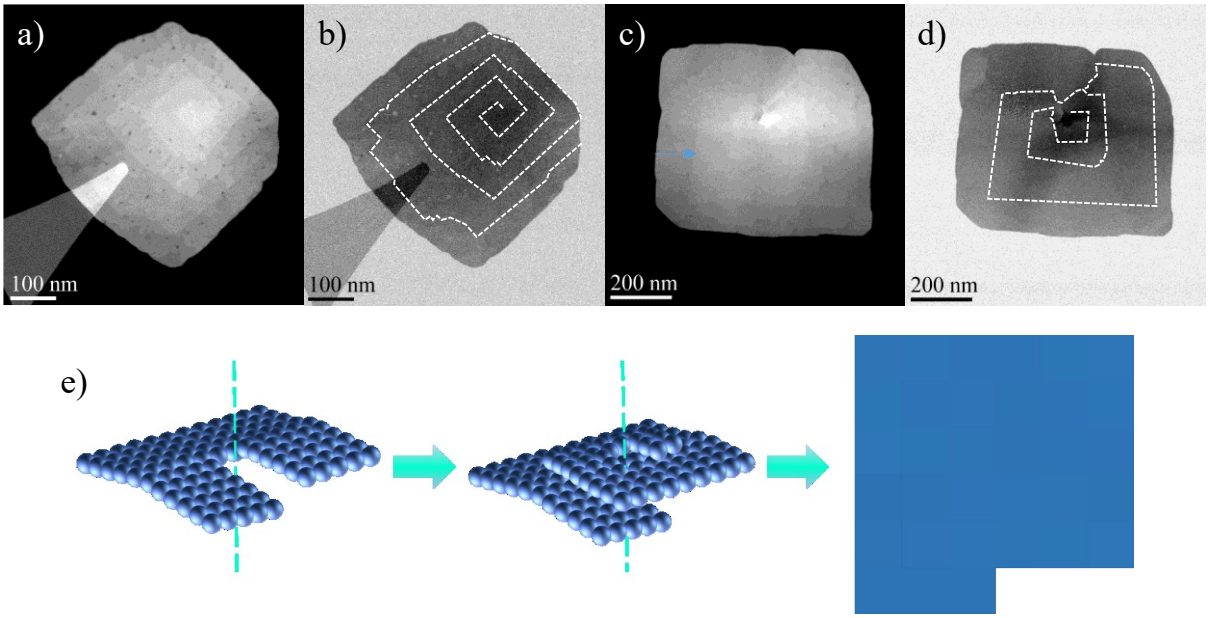

Fig. 8: a) and b): bright field and dark field STEM images of a nanopyramid. c) and d): another example. Dotted lines reproduce the spiralling edge of the pyramid. e) 3D view of steps leading to 3D-growth.

Based on the ledge mechanism, nanosheets grow through the deposition of bismuth emitted by the electrodes during the discharge, specifically on surface defects. The remarkable contribution of ions,

known to promote the 2D growth of nanoobjects [62, 63], is evident, as only the cathode surface is covered in nanosheets, while no nanoobjects are visible on the anode surface. This observation partially explains why overvoltage beyond the breakdown voltage should not be excessively high, as strong ion irradiation is known to hinder the formation of nanosheets [64]. It is also important to mention that ions here are bismuth ions. As the discharge is metallic, negative charges are electrons and those do not act the same on the anode. If ions where those of the liquid, H_3O^+ and OH^-, the main negative charge carrier in water, should play similar roles on either electrode, which is not what is observed. This mechanism is very different from Fan *et al.*'s mechanism, for instance, which is based on the ripening of dendritic nanostructures [65].

In general, the electric field streamlines are perpendicular to the electrode surfaces, favouring growth perpendicular to the surface unless influenced by local charge accumulation or space charge field effects. Although ions are known to promote anisotropic growth [62], it has been suggested that planar defects are necessary in a discharge environment to form arrays of nanosheets [63]. This finding aligns with the present study, as these planar defects correspond to the planes of combs formed during the etching step.

Thin nanosheets are believed to grow through deposition assisted by ions with moderate energy. In the early stages of the discharge, ions are highly concentrated, as the medium is considered a spark (or arc) discharge, with concentrations reaching up to 10^{17} cm^{-3} under the present conditions [56]. According to the same authors, the mean energy of these ions is low (~0.35 eV), making sputtering by these ions highly unlikely. The ions become neutralized upon reaching the cathode surface and adhere to surface defects or edges, where kinks serve as surface defects in the ledge mechanism, through surface diffusion. These defects provide the necessary excess energy for chemical bonding. Consequently, the observed vertical growth of the nanosheets is the result of the interplay between the discharge's electric field and surface defects. A schematic representation of this mechanism is depicted in **Fig. 9a**.

As elucidated by Levchenko and Ostrikov [62], nanostructures formed in discharge environments, in contrast to neutral gas-based processes, exhibit a wide range of dimensionalities and shapes, higher surface density, desired geometrical parameters, and narrower size distribution functions. This effect is primarily attributed to the strong ion focusing resulting from irregular electric fields in the nanopatterns. This focusing effectively redistributes the influx of discharge-generated building units, allowing selective control of their delivery to the growing nanostructures.

As a result, the contribution of neutral atoms produced by electrode erosion is likely to be minimal. These neutral atoms are emitted outward from the electrode tip, and it is unlikely that they reach the counter-electrode with sufficiently high concentrations to compete with ions at the cathode, even though the gap between the electrodes is only 100 µm, otherwise deposition at the anode would be possible too. It is also important to note that these neutral atoms tend to form nanoparticles when the applied voltage is sufficiently high. In the present case, nanosheets are sometimes formed with minimal or very low concentrations of nanoparticles. Consequently, the atomic ratio of metallic neutrals to ions is likely to be low as well. However, experimentally supporting this statement is challenging due to the optical thickness of the medium [11].

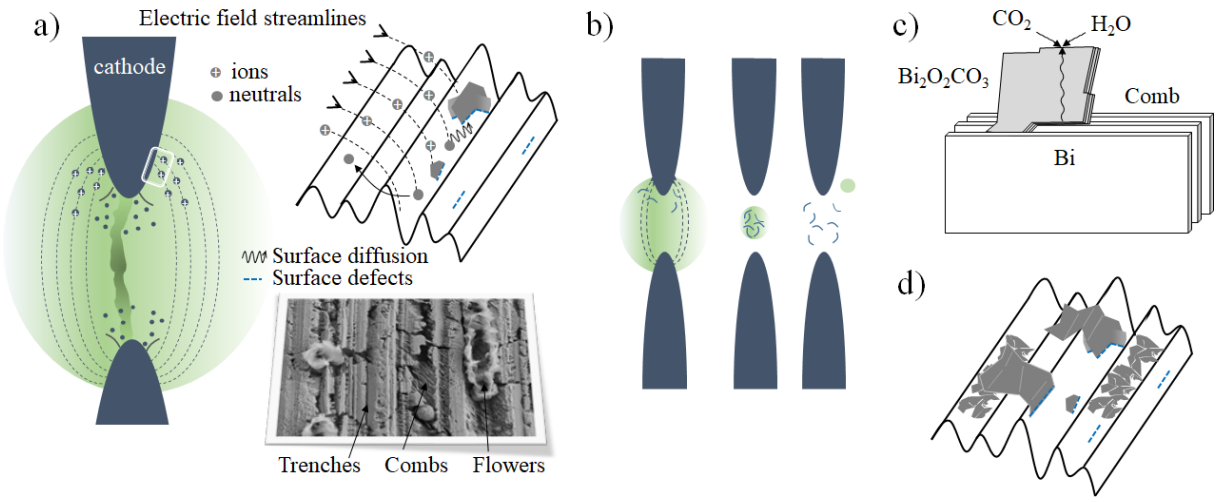

Fig. 8: Scheme of the growth mechanisms inferred from present results. *In the liquid*: a) When ions are neutralized at the cathode, they can diffuse on the surface and desorb if they do not encounter any defect. Otherwise, they contribute to growth of nanosheets. Neutral species, emitted outward from the electrode tip, do not contribute to the growth. b) Collection and ejection of nanosheets are caused by the movement of the gas-liquid interface of the discharge bubble. *In the air*: c) Bi atoms from the electrode core diffuse outwards and reach the surface where they react with H_2O and CO_2 to form $Bi_2O_2CO_3$. d) This process is activated at room temperature and kinetically slow but nanosheets can grow significantly to cover the trenches.

Once nanosheets are formed on the cathode, their collection and release in the liquid is ensured by the movement of the gas-liquid interface of the discharge bubble whose oscillations sweep the electrode surface (**Fig. 9b**). The present mechanism relies on surface processes at the cathode, providing a significant advantage by minimizing the influence of the liquid phase. This comprehensive approach paves the way for synthesizing nanosheets using different materials.

Aging in the air of electrodes leads to the synthesis of nanosheets (**Figs. 9c** and **9d**) and modify the electrode colour from metallic to white (**supplemental material 13**, **Figs. S13a** and **S13b**). This growth mechanism does not occur directly after the etching step but after the in-liquid discharge step. This means that air oxidation is activated by the discharge treatment.

Hu *et al*. [66] formed $Bi_2O_2CO_3$ nanosheets by simple hydrolysis of bismuth nanopowders through a 3-step mechanism:

$$2\ Bi + 6H_2O \rightarrow 2Bi(OH)_3 + 3H_2$$

$$Bi(OH)_3 \rightarrow BiOOH + H_2O$$

$$2BiOOH + CO_2 \rightarrow Bi_2O_2CO_3 + H_2O$$

The two last steps are the same as those proposed by Zhang *et al*. [34] for the synthesis from BiOCl, this compound being transformed into $Bi(OH)_3$ by reaction with H_2O and OH^-. This process operates at low temperature and for treatment durations that are compatible with the present observed kinetics: 60°C and 12h. As $Bi_2O_2CO_3$ is a semiconductor, we suggest that the aging process is simply governed by the outward diffusion of bismuth ions supplied by the electrode volume through the $Bi_2O_2CO_3$ nanosheets and their further oxidation by water from the air according to Zhang *et al*.'s mechanism. A schematic of this mechanism is presented in **Fig. 9c**. The process is then limited by diffusion and

nanosheets, which grow longer and longer, bend mechanically and conceal the trenches as shown in **Figs. 4b** and **9d**.

The previous process assumes that discharge activation provides access to the bismuth reservoir, which is formed by the core of not only the cathode but also the anode. Then, this step cannot be related to the ions. Discharge activation modifies the surface states of combs (**supplemental material 13, Figs. S13c** and **S13d**) and the early stage of nanosheet growth makes the surface fuzzier due to the presence of small nanosheets.

The exact role of discharges as an activation step for the air oxidation of electrodes still needs clarification. However, it is evident that an in-liquid discharge treatment is essential for this specific growth mechanism. Presumably, the discharges play a role in creating defects on emerging plans forming combs, which enable bismuth to easily access the surface. However, further experiments are required to confirm this suggestion.

Conclusion and perspective

The synthesis of nanosheets with similar characteristics can be achieved through nanosecond-pulsed discharges in both water and liquid nitrogen. To ensure successful synthesis, a low applied overvoltage slightly above the breakdown threshold is required, and the process is significantly enhanced by a suitable chemical etching pre-treatment. The selectivity of the process can be excellent, with nanosheets being the predominant nanoobjects produced without the presence of other types of nanostructures.

Nanosheets grow through localized deposition assisted by ions on the defects created by the chemical etching of the cathode electrode. Planes of combs, primarily found in trenches created by the polishing process but not limited to them, provide the necessary support for nanosheet growth. The nanosheets form flower-like structures that are randomly distributed along the trenches. The sweeping action of the bubble-liquid interface over the cathode surface collects the nanosheets, often leading to their fragmentation, and releases them into the liquid during the collapse of the bubble. This mechanism facilitates the transfer of nanoobjects to the liquid, where they can be subsequently collected.

Aging of electrodes in air after in-liquid discharge treatment makes nanosheets grow on both electrodes but with much slower rates than by discharges in liquids. Nanosheets grow by outward diffusion of bismuth from the electrode core but the way the discharge treatment activates this mechanism is still unclear. It should imply creation of defects on emerging plans in combs on both electrodes.

This study does not clarify why certain materials with low-melting points as bismuth (545 K), such as tin (melting point = 505 K) or indium (melting point = 430 K), do not form nanosheets. One possible reason for the limitation of nanosheet growth in these cases could be the absence of emerging defects. Further investigations are now required to fully understand these limitations and to extend the synthesis of nanosheets to a wider range of metals.

Acknowledgment

The authors acknowledge the French PIA (programme d'investissements d'avenir) project Lorraine Université d’Excellence (Ref. ANR-15-IDEX-04-LUE) for financial support.

References

[1] A.K. Geim, I.V. Grigorieva, Van der Waals heterostructures, Nature 499 (2013) 419–425.

[2] S.Z. Butler, S.M. Hollen, L. Cao, Y. Cui, J.A. Gupta, H.R. Gutiérrez, T.F. Heinz, S.S. Hong, J. Huang, A.F. Ismach, E. Johnston-Halperin, M. Kuno, V.V. Plashnitsa, R.D. Robinson, R.S. Ruoff, S. Salahuddin, J. Shan, L. Shi, M.G. Spencer, M. Terrones, W. Windl, J.E. Goldberger, Progress, challenges, and opportunities in two-dimensional materials beyond graphene, ACS nano 7 (2013) 2898–2926.

[3] D. Geng, H.Y. Yang, Recent advances in growth of novel 2D materials: beyond graphene and transition metal dichalcogenides, Adv. Mater. 30 (2018) 1800865.

[4] T. Belmonte, A. Hamdan, F. Kosior, C. Noël, G. Henrion, Interaction of discharges with electrode surfaces in dielectric liquids: application to nanoparticle synthesis, J. Phys. D: Appl. Phys. 47 (2014) 224016.

[5] G. Saito, T. Akiyama, Nanomaterial synthesis using plasma generation in liquid, J. Nanomat. 2015 (2015) 123696.

[6] V.S. Burakov, E.A. Nevar, M.I. Nedel'Ko, N.V. Tarasenko, Synthesis and modification of molecular nanoparticles in electrical discharge plasma in liquids. Russ. J. Gen. Chem. 85 (2015) 1222–1237.

[7] Q. Chen, J. Li, Y. Li, A review of plasma–liquid interactions for nanomaterial synthesis. J. Phys. D: Appl. Phys. 48 (2015) 424005.

[8] S. Horikoshi, N. Serpone, In-liquid plasma: A novel tool in the fabrication of nanomaterials and in the treatment of wastewaters, RSC Adv. 7 (2017) 47196–47218.

[9] N. Sano, H. Wang, M. Chhowalla, I. Alexandrou, G.A. Amaratunga, Synthesis of carbon'onions' in water, Nature 414(6863), (2001) 506–507.

[10] N. Sano, T. Kikuchi, H. Wang, M. Chhowalla, G.A. Amaratunga, Carbon nanohorns hybridized with a metal-included nanocapsule, Carbon 42 (2004) 95–99.

[11] H. Kabbara, J. Ghanbaja, C. Noël, T. Belmonte, Synthesis of Cu@ZnO core–shell nanoparticles by spark discharges in liquid nitrogen, Nano-Struct. Nano-Objects 10 (2017) 22–29.

[12] H. Kabbara, J. Ghanbaja, C. Noël, T. Belmonte, Nano-objects synthesized from Cu, Ag and $Cu_{28}Ag_{72}$ electrodes by submerged discharges in liquid nitrogen, Mater. Chem. Phys. 217 (2018) 371–378.

[13] H. Kabbara, J. Ghanbaja, A. Redjaïmia, T. Belmonte, Crystal structure, morphology and formation mechanism of a novel polymorph of lead dioxide, γ-PbO_2, J. Appl. Cryst. 52 (2019) 304–311.

[14] A. Hamdan, M. Agati, S. Boninelli, Selective Synthesis of 2D Mesoporous CuO Agglomerates by Pulsed Spark Discharge in Water, Plasma Chem. Plasma Process. 41 (2021) 433–445.

[15] G. Saito, S. Hosokai, M. Tsubota, T. Akiyama, Influence of solution temperature and surfactants on morphologies of tin oxide produced using a solution plasma technique, Cryst. Growth Des. 12 (2012) 2455–2459.

[16] X. Chen, Y. Zhou, Q. Liu, Z. Li, J. Liu, Z. Zou, Ultrathin, single-crystal WO_3 nanosheets by two-dimensional oriented attachment toward enhanced photocatalystic reduction of CO_2 into hydrocarbon fuels under visible light, ACS Appl. Mater. Interf. 4 (2012) 3372–3377.

[17] K. Furuya, Y. Hirowatari, T. Ishioka, A. Harata, Protective agent-free preparation of gold nanoplates and nanorods in aqueous $HAuCl_4$ solutions using gas-liquid interface discharge, Chem. Lett. 36 (2007) 1088–1089.

[18] M. Xiu, X. Cao, Y. Lu, K. Huang, C. Li, B. Zhang, J. Wu Y Huang, Electric-field oriented self-assembly of Mn_3O_4 nanostructures driven by liquid plasma discharge for super capacitor, Electrochim. Acta 439 (2023) 141620.

[19] J. Ding, H. Wang, Y. Luo, Y. Xu, J. Liu, Y. Lin, (002) Oriented $Bi_2O_2CO_3$ nanosheets with enhanced photocatalytic performance for toluene removal in air, Catalysts 10 (2020) 389.

[20] F. Dong, W.K. Ho, S.C. Lee, Z.B. Wu, M. Fu, S.C. Zou, Y. Huang, Template-free fabrication and growth mechanism of uniform $(BiO)_2CO_3$ hierarchical hollow microspheres with outstanding photocatalytic activities under both UV and visible light irradiation, J. Mater. Chem. 21 (2011) 12428–12436.

[21] L. Chen, R. Huang, S.F. Yin, S.L. Luo, C.T. Au, Flower-like $Bi_2O_2CO_3$: Facile synthesis and their photocatalytic application in treatment of dye-containing wastewater, Chem. Eng. J. 193–194 (2012) 123-130.

[22] T.Y. Zhao, J.T. Zai, M. Xu, Q. Zou, Y.Z. Su, K.X. Wang, X.F. Qian, Hierarchical $Bi_2O_2CO_3$ microspheres with improved visible-light-driven photocatalytic activity, CrystEngComm 13 (2011) 4010-4017.

[23] H.F. Cheng, B.B. Huang, K.S. Yang, Z.Y. Wang, X.Y. Qin, X.Y. Zhang, Y. Dai, Facile Template-Free Synthesis of $Bi_2O_2CO_3$ Hierarchical Microflowers and Their Associated Photocatalytic Activity, ChemPhysChem 11 (2010) 2167–2173.

[24] F. Dong, Y.J. Sun, M. Fu, W.K. Ho, S.C. Lee, Z.B. Wu, Novel in Situ N-Doped $(BiO)_2CO_3$ Hierarchical Microspheres Self-Assembled by Nanosheets as Efficient and Durable Visible Light Driven Photocatalyst, Langmuir 28 (2012) 766–773.

[25] B. Luo, G. Liu, L. Wang, Recent advances in 2D materials for photocatalysis. Nanoscale 8 (2016) 6904–6920.

[26] Z. Ni, Y. Sun, Y. Zhang, F. Dong, Fabrication, modification and application of $(BiO)_2CO_3$-based photocatalysts: A review, Appl. Surf. Sci. 365 (2016) 314–335.

[27] N. Tian, C. Hu, J. Wang, Y. Zhang, T. Ma, H. Huang, Layered bismuth-based photocatalysts. Coordin. Chem. Rev. 463 (2022) 214515.

[28] C. Chen, J. Ma, Z. Yi, S. Wang, H. Gao, Y. Wang, H. Yang, Highly-efficient and recyclable $Bi_2O_2CO_3$ adsorbent achieved by surfactant modification and its application in pollutant removal. Mater. Res. Bull. 159 (2023) 112091.

[29] X.D. Liang, Q.Z. Zheng, N. Wei, Y.Y. Lou, S.N. Hu, K.M. Zhao, H.G. Liao, N. Tian, Z.Y. Zhou, S.G. Sun, In-situ constructing Bi@ $Bi_2O_2CO_3$ nanosheet catalyst for ampere-level CO_2 electroreduction to formate, Nano Energy 114 (2023) 108638.

[30] J. Liu, Y. Li, Z. Li, J. Ke, H. Xiao, Y. Hou, In situ growing of Bi/$Bi_2O_2CO_3$ on Bi_2WO_6 nanosheets for improved photocatalytic performance, Catal. Today 314 (2018) 2–9.

[31] G.Y. Zhang, J.J. Wang, X.Q. Shen, J.J. Wang, B.Y. Wang, D. Z. Gao, Br-doped $Bi_2O_2CO_3$ nanosheets with improved electronic structure and accelerated charge migration for outstanding photocatalytic behavior. Applied Surface Science, 470 (2019) 63-73.

[32] B. D. Amadu, D. Xu, Q. Zhang, Z. Zhang, Q. Wang, Y. Dong, G. Zhang, Z. Ren, P. Wang, Synthesis of ultrathin, porous and surface modified $Bi_2O_2CO_3$ nanosheets by Ni doping for photocatalytic organic pollutants degradation, J. Taiwan Inst. Chem. Eng. 125 (2021) 78–87.

[33] M. Han, Y. Qian, X. Li, N. Wang, T. Song, L. Liu, X. Wang, X. Wu, M-K. Law, B. Long, Ni-doped $Bi_2O_2CO_3$ nanosheet with H^+/Zn^{2+} co-insertion for “rocking chair” zinc-ion battery, J. Colloid Interf. Sci. 645 (2023) 483–492.

[34] X. Zhang, T. Guo, X. Wang, Y. Wang, C. Fan, H. Zhang, Facile composition-controlled preparation and photocatalytic application of BiOCl/ $Bi_2O_2CO_3$ nanosheets. Appl. Catal. B: Environ. 150 (2014) 486–495.

[35] Q. Zhang, B. Xu, S. Yuan, M. Zhang, T. Ohno, Improving g-C_3N_4 photocatalytic performance by hybridizing with $Bi_2O_2CO_3$ nanosheets, Catalysis Today, 284 (2017) 27–36.

[36] X. Hu, H. Zhao, Y. Liang, F. Chen, J. Li, R. Chen, Broad-spectrum response NCQDs/ $Bi_2O_2CO_3$ heterojunction nanosheets for ciprofloxacin photodegradation: Unraveling the unique roles of NCQDs upon different light irradiation, Chemosphere 264 (2021) 128434.

[37] C. Yang, Z. Xue, J. Qin, M. Sawangphruk, S. Rajendran, X. Zhang, R. Liu, Visible light-driven photocatalytic H_2 generation and mechanism insights into $Bi_2O_2CO_3$/G-C_3N_4 Z-scheme photocatalyst, J. Phys. Chem. C 123 (2019) 4795–4804.

[38] W. Kang, B. Lin, Z. Jiang, Z. Liu, L. Feng, Y. Sun,.X. Zhang, H. Yang, G. Huang, B. Xing, C. Zhang, $Bi_2O_2CO_3$ microspheres anchored on reduced graphene oxide nanosheets as electrode material for lithium ion batteries and supercapacitors, Mater. Lett. 240 (2019) 299–302.

[39] Z. Zhao, Y. Zhou, F. Wang, K. Zhang, S. Yu, K. Cao, Polyaniline-decorated {001} facets of $Bi_2O_2CO_3$ nanosheets: in situ oxygen vacancy formation and enhanced visible light photocatalytic activity, ACS Appl. Mater. Interf. 7 (2015) 730–737.

[40] T. Li, X. Hu, C. Liu, C. Tang, X. Wang, S. Luo, Efficient photocatalytic degradation of organic dyes and reaction mechanism with Ag_2CO_3/ $Bi_2O_2CO_3$ photocatalyst under visible light irradiation, J. Molec. Catal. A: Chem. 425 (2016) 124–135.

[41] J. Zhang, Z. Liu, Z. Ma, Facile formation of $Bi_2O_2CO_3$/Bi_2MoO_6 nanosheets for visible light-driven photocatalysis, ACS Omega, 4 (2019) 3871–3880.

[42] J. Hu, D. Chen, N. Li, Q. Xu, H. Li, J. He, J. Lu, Recyclable carbon nanofibers@ hierarchical I-doped $Bi_2O_2CO_3$–MoS_2 membranes for highly efficient water remediation under visible-light irradiation, ACS Sustain. Chem. Eng. 6 (2018) 2676–2683.

[43] J. Li, M. Li, Y. Li, X. Guo, Z. Jin, Lotus-leaf-like $Bi_2O_2CO_3$ nanosheet combined with Mo_2S_3 for higher photocatalytic hydrogen evolution, Sep. Purif. Technol. 288 (2022) 120588.

[44] Y. Guo, Y., Dai, W. Zhao, H. Li, B. Xu, C. Sun, Highly efficient photocatalytic degradation of naphthalene by $Co_3O_4/Bi_2O_2CO_3$ under visible light: A novel p–n heterojunction nanocomposite with nanocrystals/lotus-leaf-like nanosheets structure, Appl. Catal. B: Environ. 237 (2018) 273–287.

[45] D. Hu, K. Zhang, Q. Yang, M. Wang, Y. Xi, C. Hu, Super-high photocatalytic activity of Fe_2O_3 nanoparticles anchored on $Bi_2O_2CO_3$ nanosheets with exposed {0 0 1} active facets, Appl. Surf. Sci. 316 (2014) 93–101.

[46] Y. Liu, Z. Wang, B. Huang, K. Yang, X. Zhang, X. Qin, Y. Dai, Preparation, electronic structure, and photocatalytic properties of $Bi_2O_2CO_3$ nanosheet, Appl. Surf. Sci. 257 (2010) 172–175.

[47] T. Gupta, N. Rosza, M. Sauer, A. Goetz, M. Winzely, J. Rath, S. Naghdi, A. Lechner, D.H. Apaydin, A. Cherevan, G. Friedbacher, A. Foelske, S.M. Skoff, B.C. Bayer, D.Eder, Sonochemical Synthesis of Large Two-Dimensional $Bi_2O_2CO_3$ Nanosheets for Hydrogen Evolution in Photocatalytic Water Splitting, Adv. Sust. Syst. 6 (2022) 2100326.

[48] H. Qin, Y. Yang, W. Shi, Y. She, Few-layer $Bi_2O_2CO_3$ nanosheets derived from electrochemically exfoliated bismuthene for the enhanced photocatalytic degradation of ciprofloxacin antibiotic, RSC Adv. 11 (2021) 13731–13738.

[49] Y. Zhang, Y. Chen, R. Liu, X. Wang, H. Liu, Y. Zhu, Q. Qian, Y. Feng, M. Cheng, G. Zhang, Oxygen vacancy stabilized $Bi_2O_2CO_3$ nanosheet for CO_2 electroreduction at low overpotential enables energy efficient CO-production of formate, InfoMat 5 (2023) e12375.

[50] T. Belmonte, A.V. Nominé, C. Noël, T. Gries, A. Nominé, V. Milichko, M. Belmahi, M. Y. Awaji, Submerged discharges in liquids for nanoobject synthesis: expectations and capabilities, Plasma Chem. Plasma Process. (2023) accepted.

[51] N. Saito, T. Ueno, M.A. Bratescu, J. Hieda, Synthesis of Nanomaterials Using Solution Plasma Process. Novel Structured Metallic and Inorganic Materials. Y. Setsuhara et al. (eds.), Novel Structured Metallic and Inorganic Materials. Springer Nature Singapore Pte Ltd. Chap 23. (2019) 343−355.

[52] T. Jedsukontorn, T. Ueno, N. Saito, M. Hunsom, Narrowing band gap energy of defective black TiO_2 fabricated by solution plasma process and its photocatalytic activity on glycerol transformation, J. Alloys Compd. 757 (2018) 188–199.

[53] A. Hamdan, C. Noel, F. Kosior, G. Henrion, T. Belmonte, Impacts created on various materials by micro-discharges in heptane: Influence of the dissipated charge, J. Appl. Phys. 113 (2013) 043301.

[54] F. Yang, A.O. Elnabawy, R. Schimmenti, P. Song, J. Wang, Z. Peng, S. Yao, R. Deng, S. Song, Y. Lin, M. Mavrikakis, W. Xu, Bismuthene for highly efficient carbon dioxide electroreduction reaction, Nat. Comm. 11 (2020) 1088.

[55] W. Lv, J. Bei, R. Zhang, W. Wang, F. Kong, L. Wang,W. Wang, $Bi_2O_2CO_3$ nanosheets as electrocatalysts for selective reduction of CO_2 to formate at low overpotential, ACS omega 2 (2017) 2561–2567.

[56] A.V. Nominé, C. Noel, T. Gries, A. Nominé, V.A. Milichko, T. Belmonte, Study by Optical Spectroscopy of Bismuth Emission in a Nanosecond-Pulsed Discharge Created in Liquid Nitrogen, Molecules 26 (2021) 7403.

[57] A. Kramida, Yu. Ralchenko, J.Reader and NIST ASD Team (2022). NIST Atomic Spectra Database (ver. 5.10), [Online]. Available: https://physics.nist.gov/asd [2023, July 3]. National Institute of Standards and Technology, Gaithersburg, MD.

[58] R.M. Tahboub, M. El Guindy, H.D. Merchant, Oxidation Kinetics of Bismuth and Its Dilute Alloys, Oxid. Met. 13 (1979) 545–556.

[59] T. Eckert, M. Schmidt, D. de Las Heras, Gravity-induced phase phenomena in plate-rod colloidal mixtures, Comm. Phys. 4 (2021) 1–13.

[60] D.A. Porter, K.E. Easterling, M.Y. Sherif, Chap. 3: Crystal Interfaces and Microstructures. In: Phase Transformations in Metals and Alloys, 3rd ed. Boca Raton: CRC Press. (2009) pp. 113-198.

[61] F.E.I. Meng, S.A. Morin, A. Forticaux, S. Jin, Screw dislocation driven growth of nanomaterials, Acc. Chem. Res. 46 (2013) 1616–1626.

[62] I. Levchenko, K. Ostrikov, Nanostructures of various dimensionalities from plasma and neutral fluxes, J. Phys. D: Appl. Phys. 40 (2007) 2308–2319.

[63] H. Zhuang, L. Zhang, R. Fuchs, T. Staedler, X. Jiang, When epitaxy meets plasma: a path to ordered nanosheets arrays, Sci. Rep. 3 (2013) 2427.

[64] M. Hori, H. Kondo, M. Hiramatsu, Radical-controlled plasma processing for nanofabrication, J. Phys. D: App. Phys. 44 (2011) 174027.

[65] H.J. Fan, R. Scholz, F.M. Kolb, M. Zacharias, U. Gösele, F. Heyroth, F., J.C. Eisenschmidt, T. Hempel, J. Christen, On the growth mechanism and optical properties of ZnO multi-layer nanosheets, Appl. Phys. A 79 (2004) 1895–1900.

[66] Y. Hu, Y. Li, C. Fan, Y. Wang, X. Zhang, Y. Wang, Simple hydrolysis route to synthesize $Bi_2O_2CO_3$ nanoplate from Bi nanopowder and its photocatalytic application, Mater. Lett. 170 (2016) 72–75.

SUPPLEMENTAL MATERIAL 1

a)

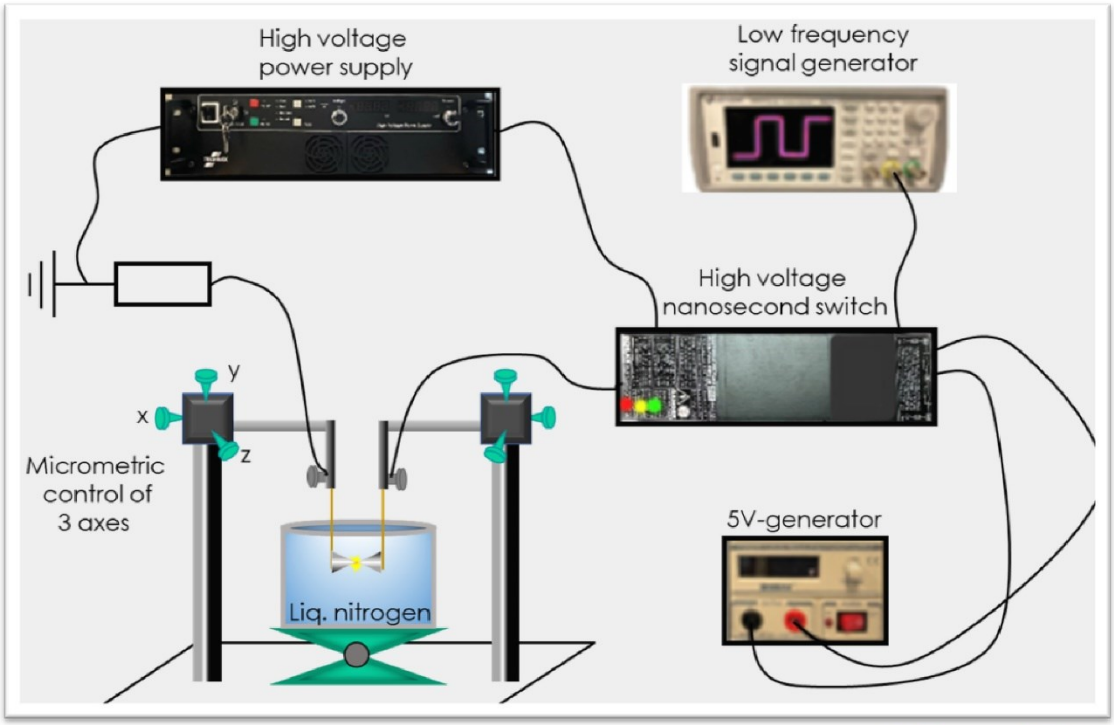

b)

c)

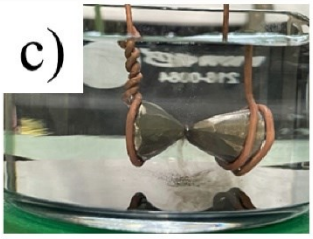

d)

Solution	Composition
Nital 4%	4 ml HNO_3 (>70 wt.%) + C_2H_5OH (100 ml)
Nital 5%	5 ml HNO_3 (>70 wt.%) + C_2H_5OH (100 ml)
Chloric-based solution	HCl (30 ml) + $FeCl_3$ (2 g) + H_2O (100 ml)
Acetic-based solution	Glacial acetic acid CH_3COOH (96wt.%) with concentrated nitric acid HNO_3

Fig. S1: a) Schematic of the experimental setup, here presented in the case of liquid nitrogen. b) Pretreatment of the electrodes leading to a cone-shaped pin etched in one of the chemical solution presented in d). c) Picture of the electrodes in milli-Q water. d) Composition of the four chemical solutions tested in this work.

SUPPLEMENTAL MATERIAL 2

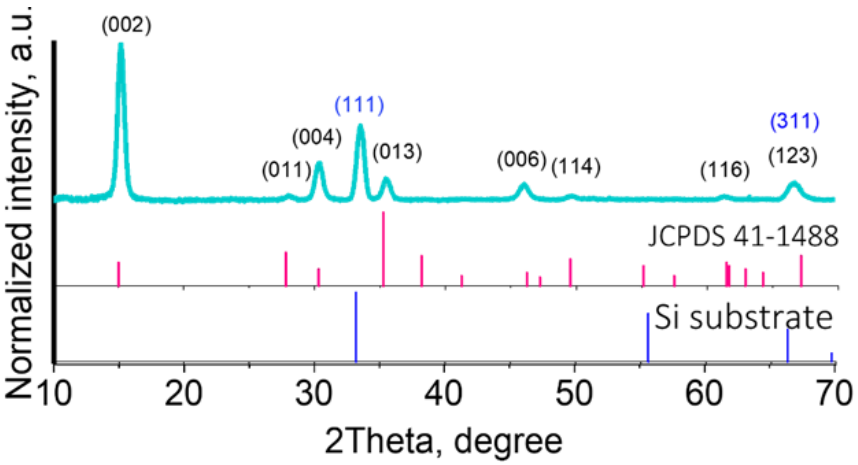

Fig. S2: XRD pattern of nanosheets deposited on a silicon wafer. Peaks in red correspond to the $Bi_2O_2CO_3$ phase (JCPDS 41-1488).

SUPPLEMENTAL MATERIAL 3

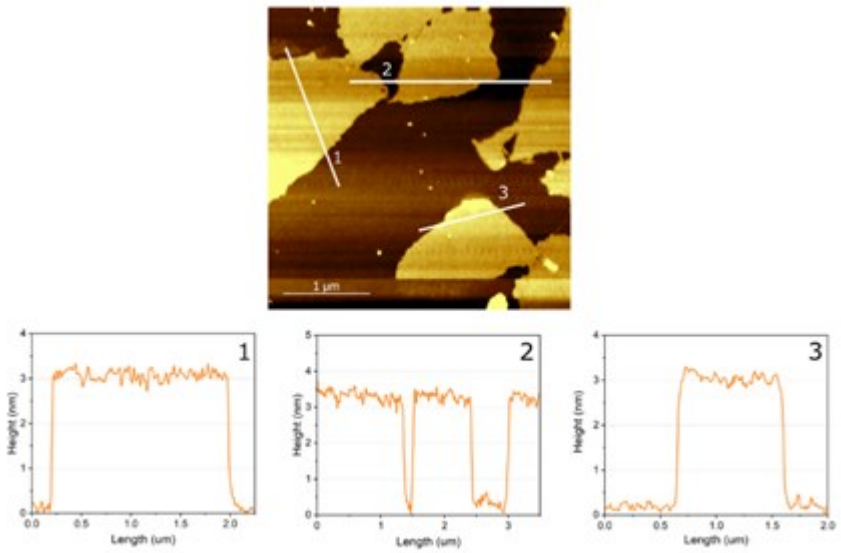

Fig. S3: AFM analysis of $Bi_2O_2CO_3$ nanosheets showing the evolution of the surface thickness of 3 individual nanosheets.

SUPPLEMENTAL MATERIAL 4

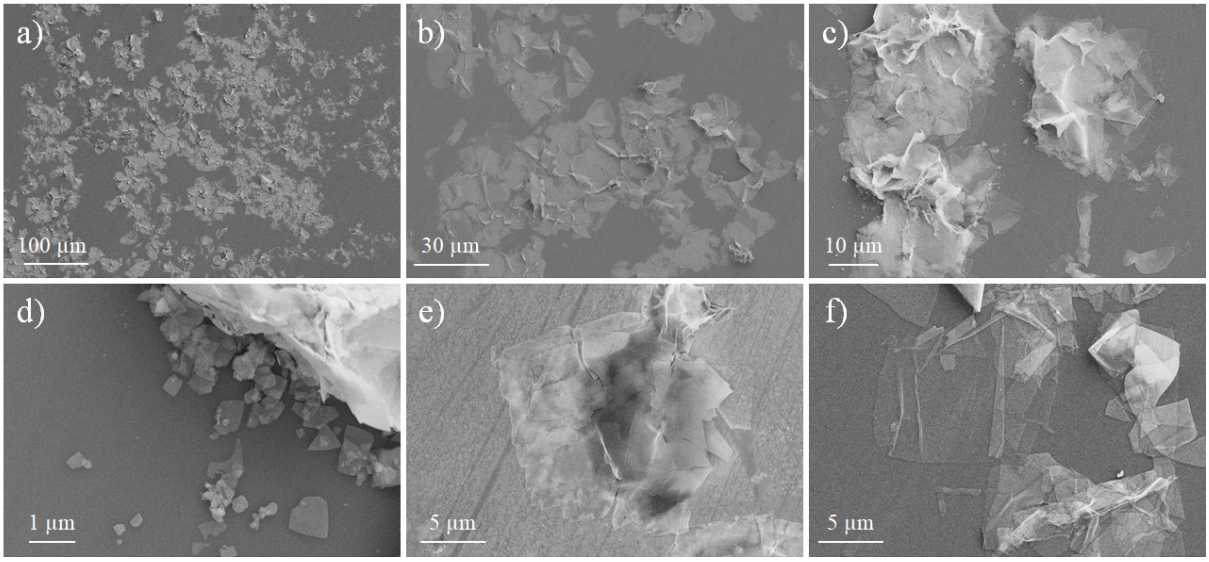

Fig. S4: Scanning electron microscope images at different magnifications (a: x180, b:x700, c: x1400) of a silicon wafer covered in nanosheets (case of water but similar images are obtained with liquid nitrogen). d) Small fragments around crumpled nanosheets. e) Broken thick nanosheets. f) ultrathin nanosheets.

SUPPLEMENTAL MATERIAL 5

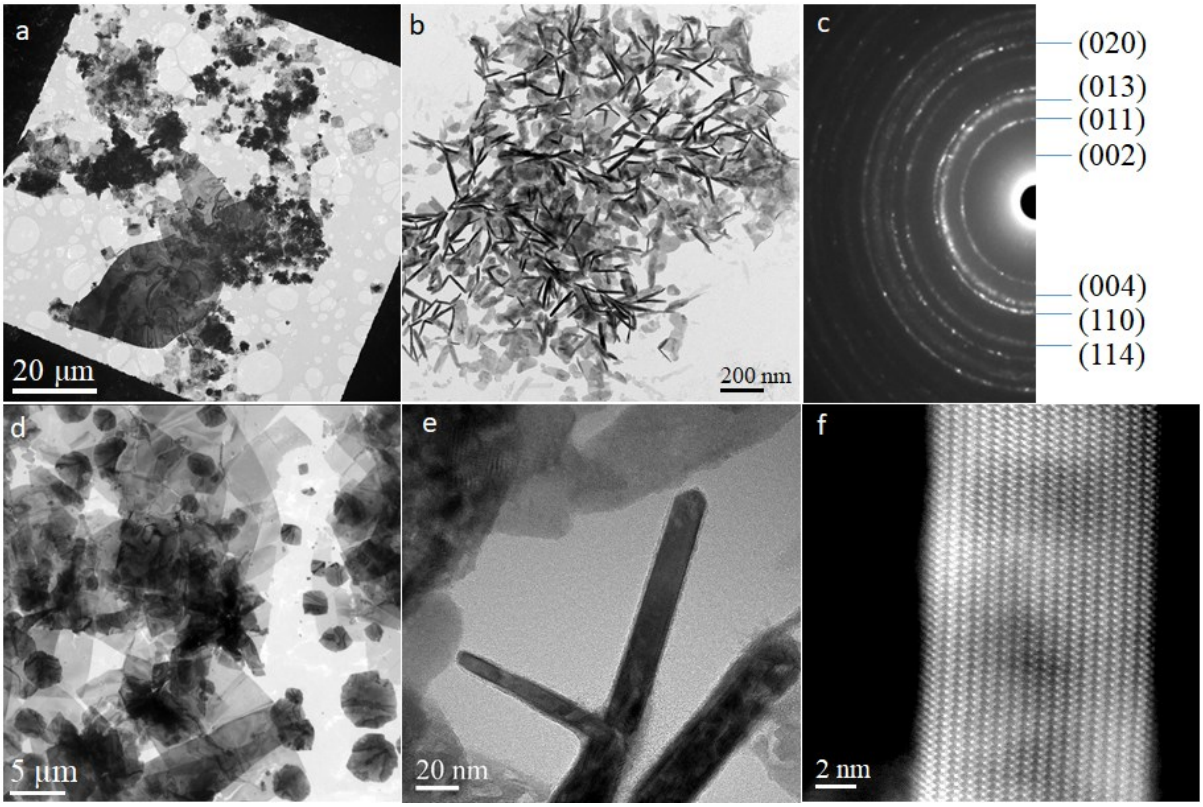

Fig. S5: a) Set of nanosheets as in Figs. 1a (water) and 1d (liquid nitrogen). b) Thin rolled nanosheets. c) Corresponding diffraction pattern and d-spacings corresponding to $Bi_2O_2CO_3$ (JCPDS card 41-1488). e) High magnification of a properly-oriented cross-section of a nanosheet. f) Atomic resolution of the corresponding structure showing the zig-zag structure of $Bi_2O_2CO_3$.

SUPPLEMENTAL MATERIAL 6

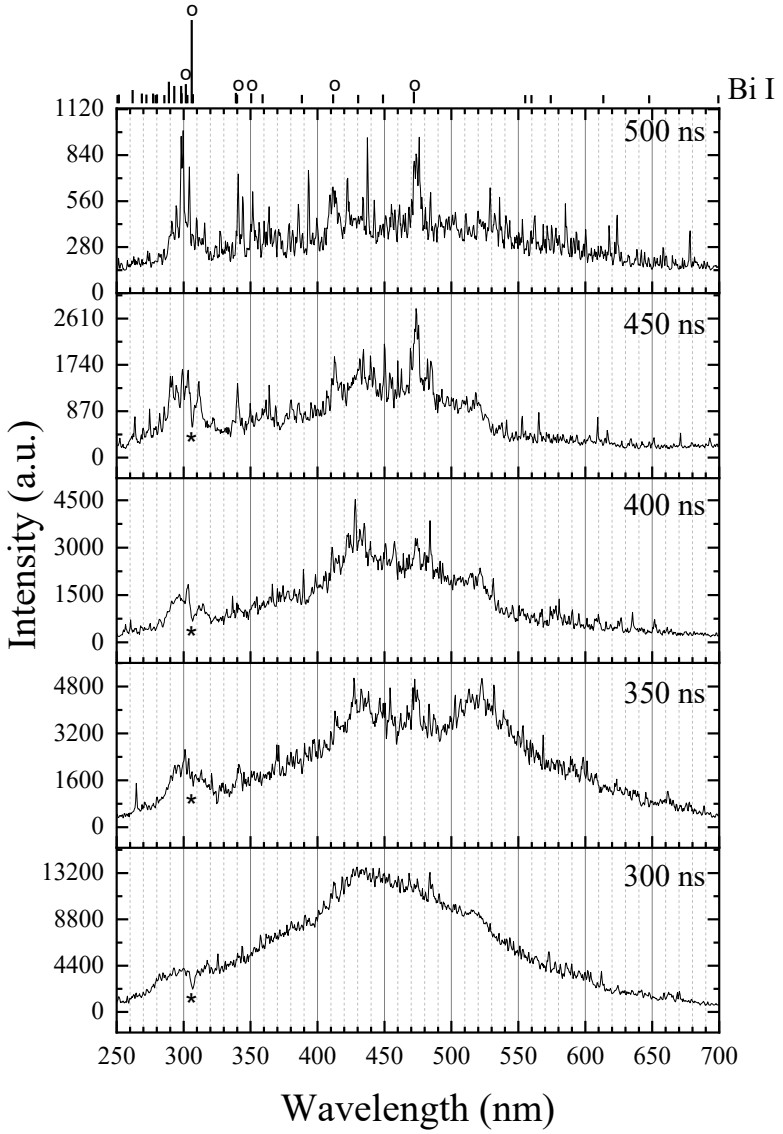

Fig. S6: Time-resolved low-resolution optical emission spectra in the visible range of a nanosecond-pulsed discharge in water created between two pin electrodes. Before 300 ns, only continua are observed. Spectra are much noisier than in liquid nitrogen. For this reason, Bi I lines that are identified for certainty are depicted by an "o" above the expected wavelengths of the possible transitions showed by bars on the top of the graph. * show absorbed lines due to absorption of photons emitted by the continuum. Wavelengths of Bi I transitions are taken from NIST [S6a].

[S6a] Kramida, A., Ralchenko, Yu., Reader, J., and NIST ASD Team (2022). *NIST Atomic Spectra Database* (ver. 5.10), [Online]. Available: https://physics.nist.gov/asd [2023, July 3]. National Institute of Standards and Technology, Gaithersburg, MD. DOI: https://doi.org/10.18434/T4W30F

SUPPLEMENTAL MATERIAL 7

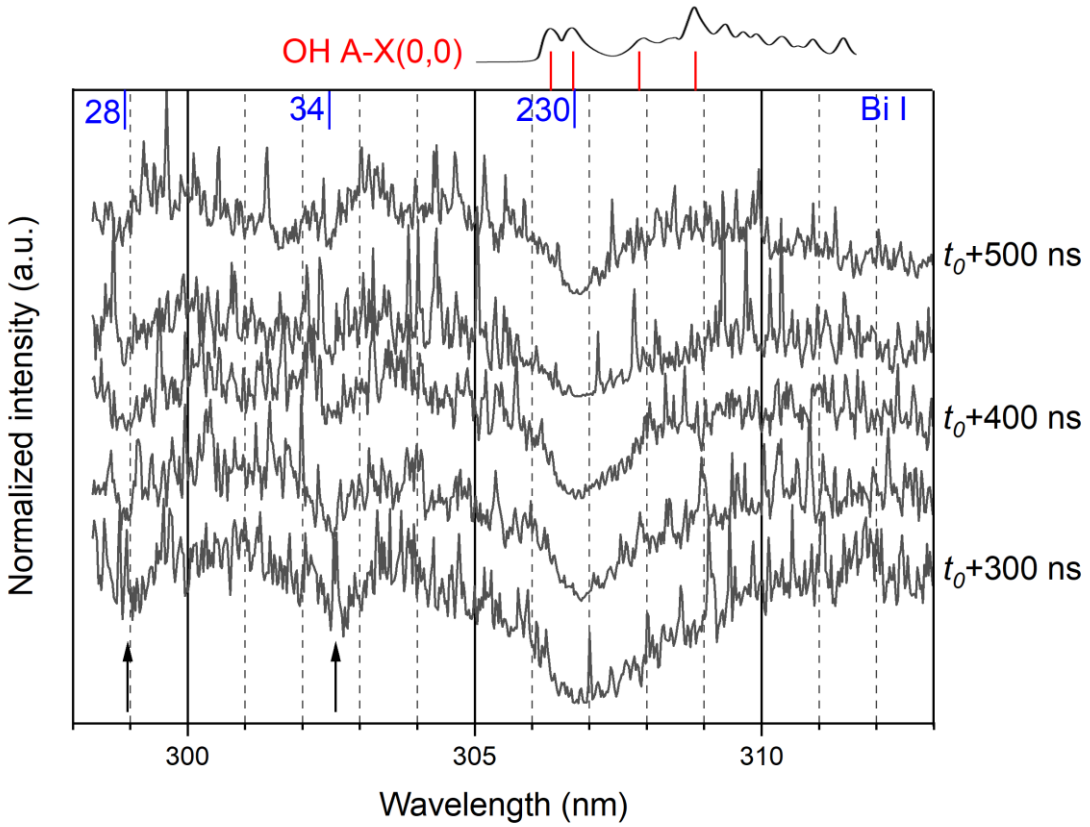

Fig. S7: High-resolution optical emission spectrum of a nanosecond-pulsed discharge in water created between two pin-electrodes made of bismuth. Grating: 1800 mm^{-1}. Acquisition time: 50 ns. Same conditions as those given in the text. Holes present in the spectrum at 298.9, 302.6 and 306.8 are attributed to Bi I self-absorption, as explained in [S5a]. 28, 34 and 230 are relative intensities from NIST database (divided by 10^3). OH emission spectrum is presented assuming a temperature of 2000 K, likely to correspond to temperature of the discharge in this period of time. If self-absorption of OH(A-X) lines was effective, other absorption bands should be visible at 307.8 and 308.9 nm. Then, it is possible to conclude that absorption is only due to bismuth and not to OH. Wavelengths of Bi I transitions are taken from NIST [S5b].

[S7a] Nominé, A. V., Noel, C., Gries, T., Nominé, A., Milichko, V. A., & Belmonte, T. (2021). Study by Optical Spectroscopy of Bismuth Emission in a Nanosecond-Pulsed Discharge Created in Liquid Nitrogen. *Molecules*, *26*(23), 7403.

[S7b] Kramida, A., Ralchenko, Yu., Reader, J., and NIST ASD Team (2022). *NIST Atomic Spectra Database* (ver. 5.10), [Online]. Available: https://physics.nist.gov/asd [2023, July 3]. National Institute of Standards and Technology, Gaithersburg, MD. DOI: https://doi.org/10.18434/T4W30F

SUPPLEMENTAL MATERIAL 8

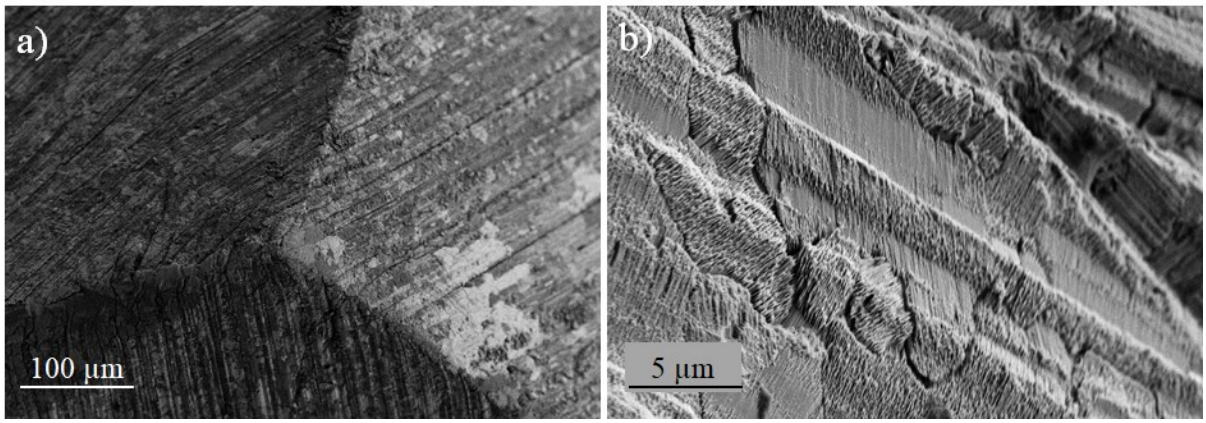

Fig. S8: Surface state of one electrode left in the air 6 days after polishing and chemical etching. a) tip of the electrode. b) Detail of trenches and combs. No nanosheets were observed.

SUPPLEMENTAL MATERIAL 9

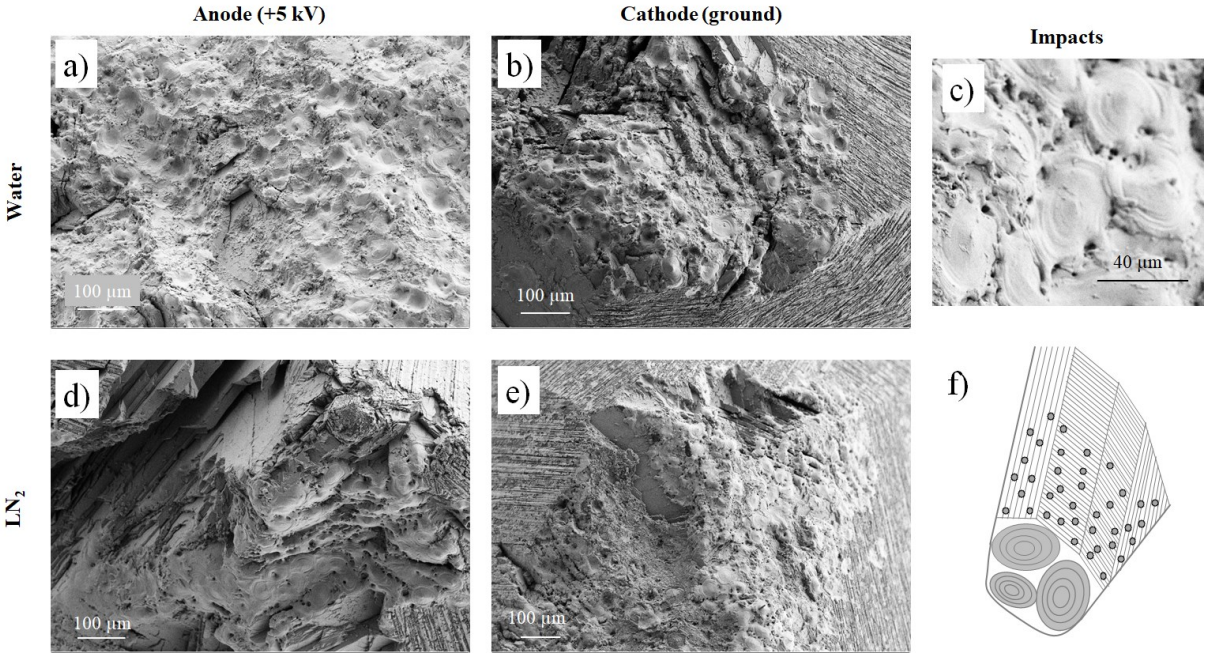

Fig. S9: Comparison of the anode and cathode tips after treatment in water (a and b) and in liquid nitrogen (d and e). The transition between the area eroded by discharges and the area etched by the Nital solution is clearly visible in b, d and f. c) Magnification showing some impacts on electrodes. f) Schematic of the electrode state after treatment. Discharge impacts are present on the electrode tip, which is dull. Lateral faces are etched and flowers are found located in the trenches, but only on the cathode.

SUPPLEMENTAL MATERIAL 10

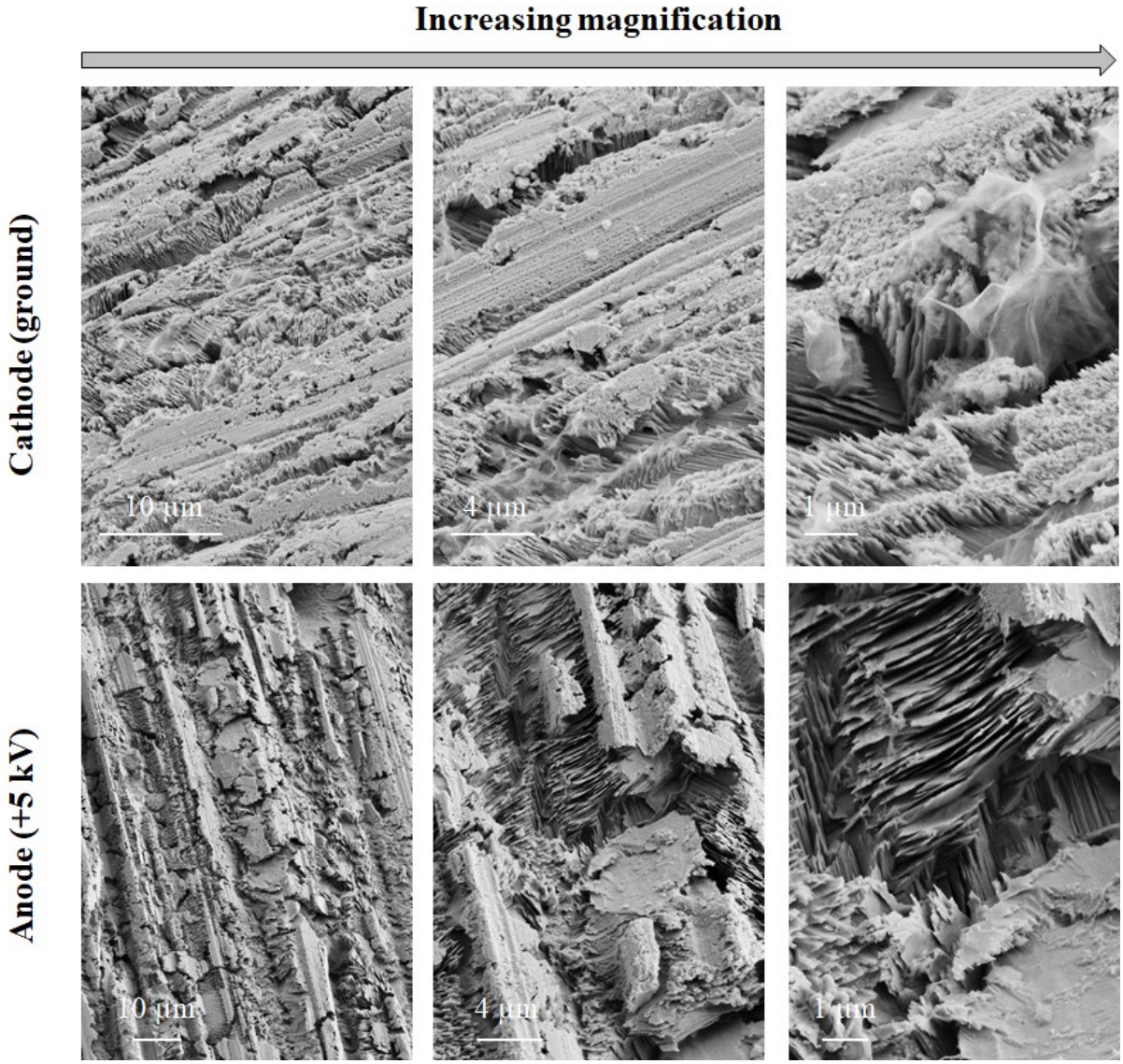

Fig. S10: Comparison of the surfaces of anode and cathode after treatment in water. The same features (trenches and combs) are observed. Here again, nanosheets are only observed on the cathode, whichever the liquid.

SUPPLEMENTAL MATERIAL 11

Fig. S11: Set of pictures showing the movement of the generated particles in the liquid between two discharges. The time scale is in second. Particles remain at the bottom of the beaker, settling by gravity.

SUPPLEMENTAL MATERIAL 12

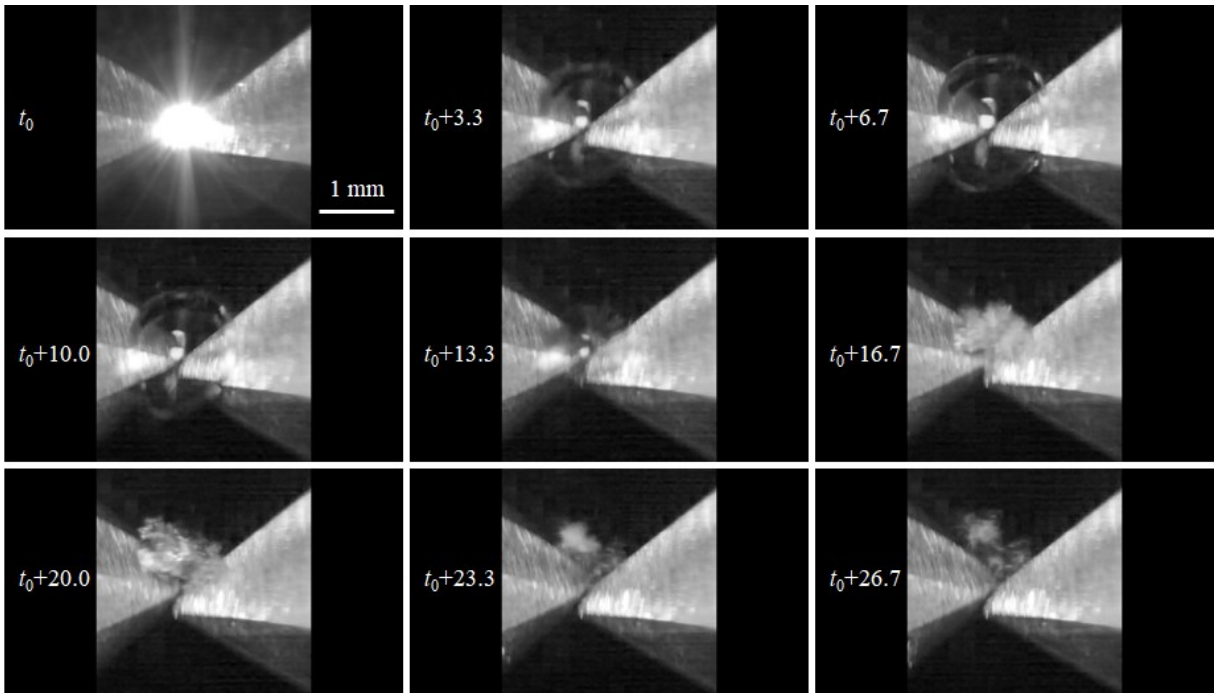

Fig. S12: Set of pictures showing the transfer of nanosheets by mechanical sweeping of the surface by the bubble-liquid interface. The time scale is in µs. Discharge conditions are those reported in the experimental part. This event is characterized by the fact that the bubble expands and collapses one time only.

SUPPLEMENTAL MATERIAL 13

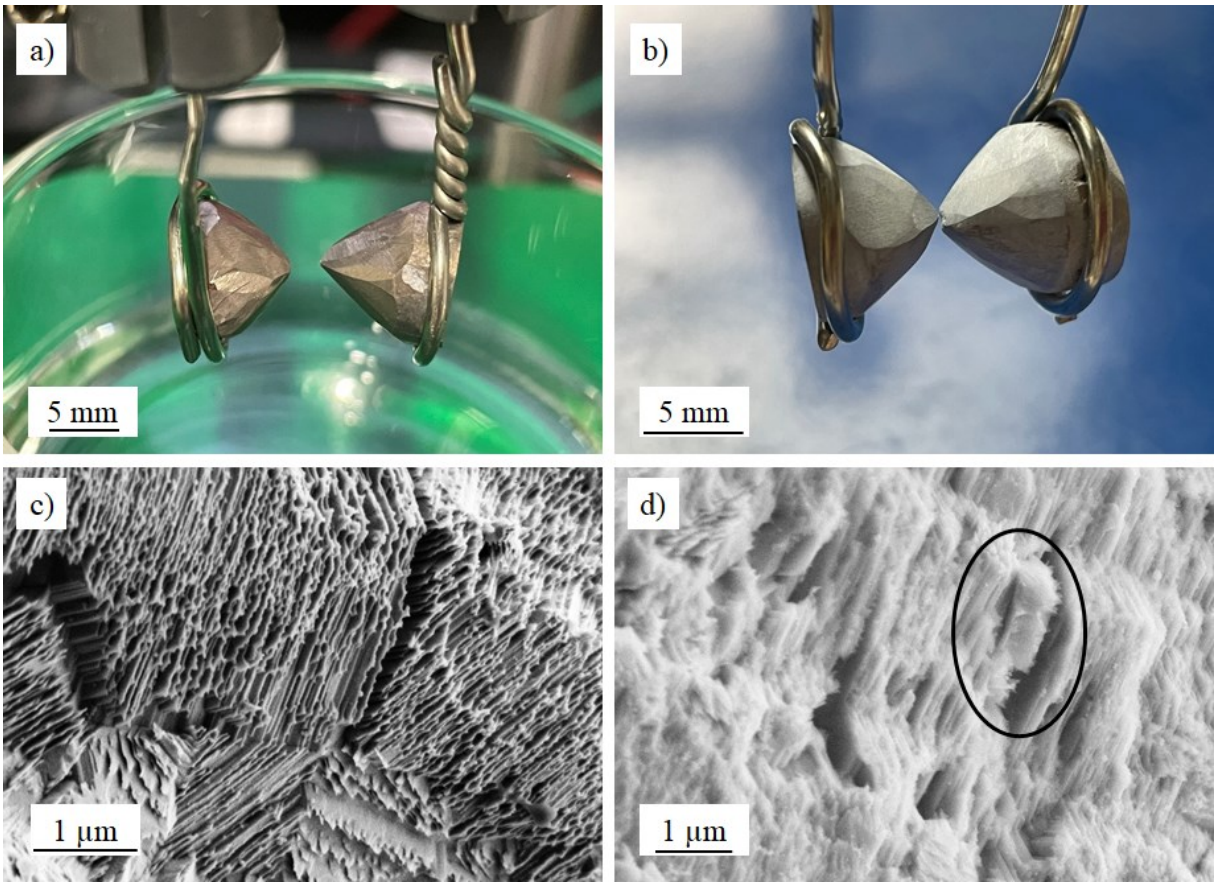

Fig. S13: a) Overall view of bismuth electrodes after polishing, chemical etching and air exposure. The metallic aspect of the electrode surface is clear. b) Same as a) but with an additional 1-min plasma activation after chemical etching. The whitish color of both electrodes is patent. c). Comb structure after polishing, chemical etching and air exposure. d) Same as c) but with an additional 1-min plasma activation after chemical etching. The encircled area shows the early stage of nanosheet growth. Note that the entire surface appears fuzzier.